RSC Advances

PAPER

Published on 09 July 2026

Cite this: *RSC Adv.*, 2026, **16**, 39458

Effect of 1*H*-benzotriazole–CeO_2 NPs hybrid inhibitors on the corrosion protection of carbon steel in chloride solutions

Safa Salmi,[a] Hichem Boudellioua, *[bc] Youcef Hamlaoui[c] and Michele Fedel[d]

Received 9th April 2026
Accepted 4th July 2026

DOI: 10.1039/d6ra03006h

rsc.li/rsc-advances

In this study, 1*H*-benzotriazole (1*H*-BTA) and cerium oxide (CeO_2) nanoparticles were investigated as corrosion inhibitors for A1008 low carbon steel in 3.5% NaCl solution. Short-term immersion tests showed that CeO_2 NPs achieved an inhibition efficiency of 73.35% at 0.3%, while 1*H*-BTA reached 74.13% at 2.5 mmol L^{-1}. Remarkably, their combined use significantly enhanced corrosion protection, yielding an efficiency of 93.46% with 2.5 mmol L^{-1} 1*H*-BTA and 0.2% CeO_2 NPs. The 1*H*-BTA–CeO_2 NPs hybrid inhibitors induced a positive shift in corrosion potential relative to the untreated steel, reflecting more anodic behavior, and simultaneously suppressed both anodic and cathodic reactions, consistent with a mixed inhibition mechanism. This was accompanied by a marked reduction in corrosion current density and a substantial improvement in corrosion resistance. Surface analysis revealed that the 1*H*-BTA–CeO_2 NPs hybrid inhibitors produced a homogeneous, crack-free film enriched in Ce and N, confirming its strong barrier properties. During long-term immersion, the composite maintained a high inhibition efficiency of 92.90%, outperforming 1*H*-BTA (85.56%) and CeO_2 NPs (45.09%), thereby highlighting the pronounced positive effect of the hybrid system. Thermodynamic analysis further indicated that the adsorption of CeO_2 NPs, 1*H*-BTA, and the 1*H*-BTA–CeO_2 hybrid on the carbon steel surface proceeds through a mixed physisorption–chemisorption mechanism.

1. Introduction

Carbon steel is extensively used across various industrial sectors due to its excellent mechanical properties, low cost, favorable physical characteristics, and ease of fabrication.[1–4] However, its performance is significantly compromised in corrosive environments, particularly those containing chloride ions, where surface rust becomes unstable and prone to localized corrosion.[5] This degradation limits its range of applications and service life. As a major societal issue, metallic corrosion represents a pervasive hazard with serious consequences, including compromised public safety, significant economic losses, and considerable environmental pollution.[6–9] Confronting these multifaceted challenges demands the development of robust corrosion protection methods. This necessity is driven by the substantial, and indeed global, economic burden imposed by corrosion processes.

To mitigate corrosion, several protection strategies have been explored, including coatings and corrosion inhibitors.[10,11] In recent years, corrosion inhibitors have gained particular attention due to their affordability, ease of application, compatibility with other materials, and effective performance under various environmental conditions. Historically, chromate and phosphate based inhibitors; especially those containing Cr^{3+} and Cr^{6+}; were widely employed due to their high efficacy.[12] However, their high toxicity and carcinogenic nature have led to strict regulatory bans,[13] driving the search for environmentally friendly alternatives.[11,14,15] Among these alternatives, rare earth elements have emerged as promising candidates for corrosion protection and surface treatment, drawing increasing scientific interest.[16]

In parallel, Benzotriazole (BTA) has established itself as a sustainable and widely used organic corrosion inhibitor.[17] Benzotriazole (BTA) is a widely recognized corrosion inhibitor, particularly for copper and its alloys, and is regarded as one of the most effective heterocyclic inhibitors. Its corrosion-inhibiting performance has been extensively studied,[18–22] along with its ability to form sparingly soluble coordination complexes with cations of various metals, including Ag, Cu, Zn, Fe, Ni, Co, and Pb.[22,23]

According to the literature,[24–26] the formation of a BTA-based inhibitory layer relies on a donor–acceptor interaction between the BTA molecule and surface iron atoms. More specifically,

[a]*Laboratory of Environmental Engineering, Department of Process Engineering, Badji Mokhtar Annaba University, 23000, Annaba, Algeria*

[b]*Department of Process and Energy Engineering, National Higher School of Technology and Engineering, 23005, Annaba, Algeria. E-mail: h.boudellioua@ensti-annaba.dz*

[c]*Laboratory of Physics of Matter and Radiation (LPMR), Faculty of Science and Technology, University Mohamed Cherif Messaadia, Souk Ahras 1553-41000, BP, Algeria*

[d]*Department of Industrial Engineering, University of Trento, via Sommarive n 9, 38123, Trento, Italy*

Table 1 Systematic comparison between CeO_2/1*H*-benzotriazole (BTA) systems incorporated into protective coatings and CeO_2/Ce^{3+} directly introduced into the corrosive solution, based on the three most relevant studies reported in the literature

Parameter	Yang *et al.*[39]	Han *et al.*[38]	Salmi *et al.*[41]
System type	In coating (encapsulated BTA)	In coating (mixed fillers)	In solution (direct inhibition)
BTA location	Inside CeO_2 nanocontainers	Dispersed in epoxy matrix	Dissolved in NaCl electrolyte
CeO_2 location	Nanocontainer shell	Filler in coating	Suspended nanoparticles
Transport mechanism	pH-triggered release + diffusion	Diffusion through coating	Direct solution diffusion
CeO_2 function	Container + Ce^{3+} source	Physical barrier	Inhibitor particle + Ce^{3+} source
Primary inhibition	Self-healing at defects	Barrier + chemical	Direct adsorption + film formation
BTA adsorption	Chemical + physical on CeO_2	Chemical on steel	Direct on steel surface

BTA is a heterocyclic compound containing three nitrogen atoms, which confer high reactivity toward metallic surfaces. These nitrogen atoms possess lone electron pairs capable of donating electrons, while the vacant orbitals of iron atoms can accept them. This interaction leads to the formation of chemical bonds between BTA and the metal surface [Fe–N]. When the molecules are arranged in an orderly manner on the surface, they form a continuous protective film capable of significantly slowing corrosion processes over the entire metal surface.

The corrosion inhibition mechanism of benzotriazole (BTA) involves the adsorption of BTA molecules onto the metal surface, leading to the formation of a protective film that suppresses electrochemical corrosion processes. However, its effectiveness on iron-based metals remains limited, even at relatively high concentrations.[11] Furthermore, although initially effective, the stability of the protective film may decrease over time.

The limited durability of BTA on steel surfaces is mainly attributed to the instability and incomplete coverage of the adsorbed film. In chloride-rich environments, competitive adsorption between BTA molecules and chloride ions can result in film discontinuities, localized breakdown, and a progressive loss of corrosion protection. Even at relatively high concentrations, the long-term stability of BTA-derived films remains insufficient for demanding applications. To overcome these limitations, recent strategies have focused on combining organic inhibitors with inorganic additives to enhance film compactness and stability.

BTA can be used alone or in combination with inorganic additives,[27,28] forming a protective complex on metal surfaces that plays a crucial role in inhibiting corrosion.[29–31] Bokati et *al.*[32] evaluated BTA's performance, both alone and in combination with $Na_2MoO_4 \cdot 2H_2O$ and $Na_3PO_4 \cdot 12H_2O$, on single and coupled copper and mild steel specimens in artificial seawater. Their findings showed that the multicomponent system significantly enhanced corrosion resistance compared to BTA alone. Further, the adsorption behavior of 1*H*-BTA on various metals revealed that it follows physisorption on mild steel and aluminum; conforming to Langmuir and El–Awady isotherms; and chemisorption on copper, consistent with the Langmuir isotherm.[31] On carbon steel, BTA forms a 2 nm thick polymer-like iron-azole film comprising Fe–triazole donor–acceptor bonds, effectively inhibiting both uniform and localized corrosion, even in the presence of chloride ions.[33]

On the other hand, cerium oxide (CeO_2), a rare earth compound, is widely used due to its ability to shift between Ce^{4+} and Ce^{3+} oxidation states, a property that underpins its effectiveness in various applications.[34] Numerous studies have highlighted CeO_2's potential as a corrosion inhibitor.[35,36] It is also commonly used as an additive to enhance protective coatings. For instance, Zhang et *al.*[37] developed a superhydrophobic, self-healing silane coating embedded with BTA-loaded hollow CeO_2 nanocapsules for copper surfaces. The coating demonstrated excellent anti-corrosion performance and self-healing capability in a 1 mol L^{-1} NaCl solution, achieving a BTA release rate of 91% within 8 hours. Similarly, previous works[38,39] incorporated both CeO_2 and BTA into an epoxy resin to protect carbon steel in 3.5% NaCl solution. In these coating systems,[38,39] BTA is either encapsulated in CeO_2 nanocontainers or dispersed as a filler within a solid epoxy matrix. The inhibition process involves slow diffusion of BTA through the coating (hours to days), pH-triggered release from containers,[38] or gradual migration to the coating/substrate interface.[39] CeO_2 acts primarily as a physical barrier or controlled-release reservoir. In both cases, the composite showed superior corrosion resistance.

Three previous studies very closely related to the present work were identified. Table 1 provides a systematic comparison between the incorporation of CeO_2/1*H*-benzotriazole (BTA) into coating matrices and their direct application as corrosion inhibitors in solution.

In this study, 1*H*-benzotriazole (1*H*-BTA) and chemically synthesized cerium oxide (CeO_2) NPs are investigated as corrosion inhibitors for low carbon steel immersed in a 3.5% NaCl solution. The inhibitors are first applied individually, followed by their combination as a 1*H*-BTA–CeO_2 NPs system. Corrosion performance is evaluated over both short and long term immersion periods, up to two weeks, to assess potential synergistic effects and overall protection efficacy. The corrosion protection provided by the combined 1*H*-BTA and CeO_2 NPs is has not yet been extensively explored. To carry out this work, the electrochemical behavior of the inhibitors is examined using potentiodynamic polarization technique, and electrochemical impedance spectroscopy (EIS). In addition, surface and structural characterizations are conducted using scanning electron microscopy (SEM) coupled with energy-dispersive spectroscopy (EDS), energy-dispersive X-ray (EDX) elemental mapping, optical microscopy (OM), and X-ray diffraction (XRD).

2. Materials and experimental Procedures

2.1. Specimen and solution preparation

Table 2 shows the chemical composition of the A1008 carbon steel sheets (Q-Panels) used in this study. These sheets were machined into cylindrical specimens with a diameter of 1.13 cm. Each specimen was connected to a copper wire at one end to ensure electrical contact, then embedded in epoxy resin, leaving a 1 cm^2 circular surface exposed to act as the working electrode in a conventional three-electrode electrochemical cell. Before each test, the exposed steel surfaces were mechanically polished using silicon carbide (SiC) abrasive papers with progressively finer grits, ranging from #320 to #4000, to achieve a smooth finish.

The samples were then cleaned through a series of steps: rinsing with distilled water, degreasing with acetone, pickling in 2 M hydrochloric acid (HCl), and rinsing again with demineralized water. Finally, they were dried using a nitrogen (N_2) airflow to eliminate any residual moisture. This surface preparation was carried out immediately prior to immersion to prevent contamination or oxidation.

Electrochemical measurements were carried out in a 3.5 wt% sodium chloride [NaCl] (Sigma-Aldrich, $M_w = 58.44$; purity 99%) were solution at its natural pH of around,[6,8] which served as the corrosive medium. A 3.5 wt% NaCl solution was selected as the test medium because it is an industry-standard electrolyte widely used to simulate the average salinity of natural seawater in laboratory corrosion studies and to evaluate the corrosion behavior of metallic materials and the performance of corrosion inhibitors in chloride-containing environments.[40]

To improve corrosion resistance, cerium oxide nanoparticles (CeO_2), synthesized from cerium nitrate [$Ce(NO_3)_3 \cdot 6H_2O$] (Sigma-Aldrich, $M_w = 434.22$; purity 99.9%) based on our previous work,[41] and 1*H*-benzotriazole (1*H*-BTA) [$C_6H_5N_3$] (Sigma-Aldrich, $M_w = 119.12$; purity 99%) were used as corrosion inhibitors (see Fig. 1). During electrochemical testing, the solution was gently stirred to create a mild vortex, enhancing natural aeration and ensuring uniform mass transport throughout the electrolyte.

Table 2 Chemical composition of A1008 low carbon steel

Elements	C	Mg	P	S	Fe
wt%	≤0.15	≤0.6	≤0.03	≤0.035	In balance

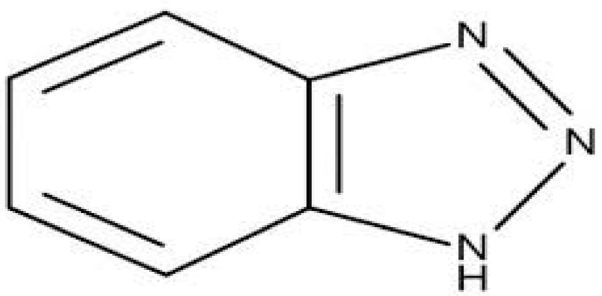

Fig. 1 Chemical structure of 1*H*-benzotriazole molecule (1*H*-BTA).

2.2. Electrochemical measurements

Electrochemical measurements were conducted using a conventional three-electrode setup. All electrodes were immersed to approximately the same depth in a 100 mL electrochemical cell containing the test solution. The A1008 carbon steel specimen served as the working electrode, platinum was used as the counter electrode, and an Ag/AgCl (3 M KCl) electrode functioned as the reference. The system was controlled using a potentiostat/galvanostat (Ametek VersaSTAT 4). Both stationary and dynamic electrochemical techniques were employed, including electrochemical impedance spectroscopy (EIS) and potentiodynamic polarization measurements. Corrosion behavior was analyzed using EC-Lab software, while EIS data were further processed with ZView simulation software. EIS measurements were performed using a low-amplitude sinusoidal signal of 5 mV, applied over a frequency range from 10^{-2} to 10^5 Hz. Potentiodynamic polarization tests were carried out within a potential window of ±0.25 V at a scan rate of 0.5 mV s^{-1}. All experiments were conducted with a constant solution volume.

Prior to each measurement, the working electrode was immersed for 30 minutes to achieve a steady-state condition, then exposed to varying concentrations of 1*H*-benzotriazole (1*H*-BTA), CeO_2 NPs, and their combination (1*H*-BTA–CeO_2 NPs). Additional long-term experiments were conducted over immersion periods of up to 14 days using the optimal concentrations of each inhibitor system. All corrosion tests were repeated three times or more to ensure reproducibility.

2.3. Surface morphology and films characterization

The composition and morphology of the surface films formed on the carbon steel after corrosion inhibition tests were evaluated using the optimal concentrations of 1*H*-BTA, CeO_2 NPs, and their combination (1*H*-BTA–CeO_2 NPs). A range of analytical techniques was employed, including Optical Microscope, Scanning Electron Microscopy (SEM, JEOL JSM IT300) coupled with Energy-Dispersive Spectroscopy (EDS), and elemental mapping. Additional characterization was performed using X-ray Diffraction (XRD). XRD analysis was carried out using an Italstructures IPD3000 diffractometer equipped with a copper anode (Cu Kα) source. Measurements were performed in reflection geometry with a fixed incident angle (omega) of 5°. Diffraction data were collected using an Inel CPS120 detector, covering a 2θ range of 20–80° with a resolution of 0.03° per channel.

2.4. Synthesis and characterization of CeO_2 NPs

CeO_2 NPs were synthesized using a co-precipitation method previously reported in our earlier studies.[41] Briefly, $Ce(NO_3)_3 \cdot 6H_2O$ was dissolved in deionized water and mixed with acetic acid under continuous stirring. The solution pH was then adjusted to 8–9 by the dropwise addition of NH_4OH, resulting in

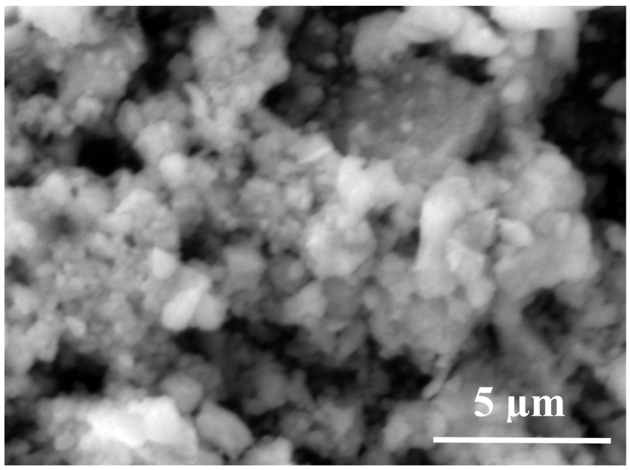

Fig. 2 SEM image of CeO_2 NPs synthesized in the presence of acetic acid.

the precipitation of $Ce(OH)_4$. The resulting suspension was maintained at 90 °C for 24 h, after which it was centrifuged and thoroughly washed with ethanol and deionized water. The precipitate was subsequently dried at 80 °C for 24 h and finally re-dispersed in water to obtain a 10 wt% colloidal suspension.

CeO_2 NPs were synthesized in-house to ensure precise control over their physicochemical properties, thereby improving the reproducibility and consistency of the experimental investigations. This approach also enabled comprehensive characterization of the nanoparticles, allowing their properties to be directly correlated with the observed performance. In contrast, commercially available CeO_2 NPs may exhibit lot-to-lot variability and limited dispersion stability in aqueous media, potentially compromising the reliability and reproducibility of experimental results.[42]

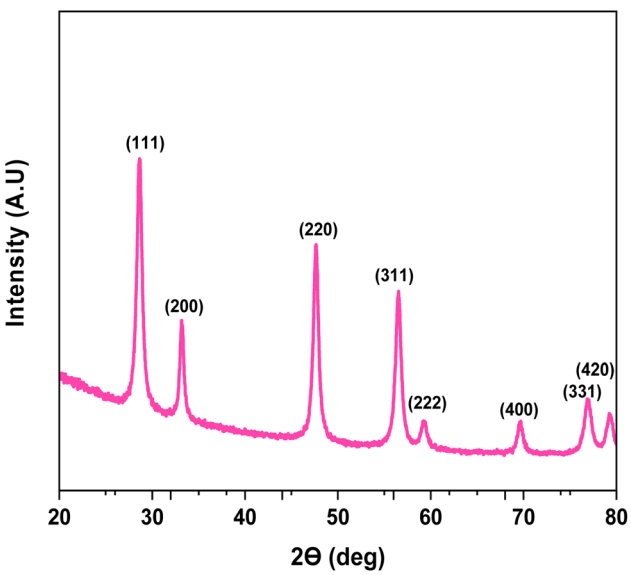

Fig. 3 XRD patterns of CeO_2 NPs synthesized in the presence of acetic acid.

The SEM analysis shown in Fig. 2 indicates that the synthesized CeO_2 NPs predominantly exhibit an irregular spherical morphology with limited agglomeration due to van der Waals interactions. Most particles are well dispersed, confirming effective synthesis and acid stabilization, while faceted edges observed at high magnification verify their cubic fluorite structure and crystalline nature.

To further confirm this structure, X-ray diffraction (XRD) analysis was performed on CeO_2 NPs synthesized from cerium nitrate dissolved in acetic acid, followed by calcination at 80 °C for 24 h. The diffraction angle (2θ) was scanned over a range of 20° to 80°. The XRD results presented in Fig. 3 confirmed the formation of the cubic fluorite phase of CeO_2, with an average crystallite size of 12.8 nm, calculated using the Debye–Scherrer equation (eqn (1)),[43] where K is a constant (0.89), λ is the wavelength of the incident radiation (1.54 Å), θ is the diffraction angle, and β is the full width at half maximum (FWHM).

$$D = \frac{k\lambda}{\beta \cos \theta} \quad (1)$$

3. Results and discussion

3.1. Effect of 1*H*-BTA and CeO_2 NPs concentrations and their combination system

3.1.1. Electrochemical behavior. Fig. 4 presents the potentiodynamic polarization curves recorded after 30 minutes of immersion in a 3.5 wt% NaCl solution at room temperature, both in the absence and presence of corrosion inhibitors (1*H*-BTA, CeO_2 NPs and 1*H*-BTA–CeO_2 NPs system). The corresponding electrochemical parameters extracted from these curves are summarized in Table 3.

The polarization resistance (R_p) values were calculated using Ohm's law (eqn (2)), based on the linear polarization plots. The corrosion current density (I_{corr}) was determined using the Stern-Geary method, as shown in eqn (3) and (4), where β_a and β_c represent the anodic and cathodic Tafel slopes, respectively.[44] The inhibition efficiency was calculated from polarization measurements using eqn (5), where I_{corr} and I_{inh} correspond to the corrosion current densities in the absence and presence of the inhibitors, respectively.[45]

$$R_p = \left(\frac{\Delta E}{\Delta I}\right) \quad (2)$$

$$I_{corr} = \frac{\beta_a \cdot \beta_c}{2.303 \cdot (\beta_a + \beta_c) \cdot R_p} \quad (3)$$

$$I_{corr} = \frac{\beta_a}{2.303 \cdot R_p} \quad (4)$$

$$E\% = \frac{I_{corr} - I_{inh}}{I_{corr}} \quad (5)$$

Fig. 4a displays the potentiodynamic polarization curves obtained with and without varying concentrations of 1*H*-BTA, ranging from 0.5 to 3.5 mmol L^{-1}. The results show a shift in

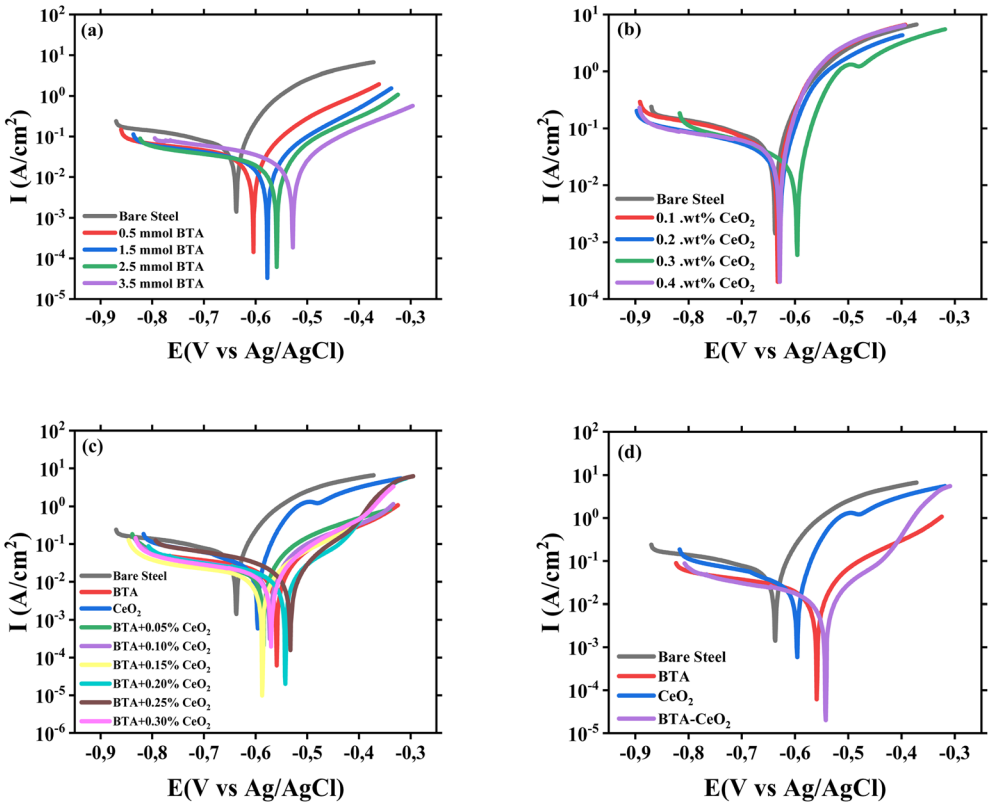

Fig. 4 Potentiodynamic polarization curves of carbon steel in 3.5 wt% NaCl at room temperature, showing the effect of: (a) increasing BTA concentrations, (b) increasing CeO_2 NPs concentrations, (c) varying CeO_2 concentrations at the optimal 1*H*-BTA concentration, and (d) a comparison of optimal concentrations of 1*H*-BTA, CeO_2 NPs, and their combination after 30 minutes of immersion.

the corrosion potential (E_{corr}) toward more anodic values with increasing inhibitor concentration. This anodic shift, along with a noticeable decrease in both anodic and cathodic current densities, indicates that 1*H*-BTA exhibits mixed-type inhibition behavior with a predominantly anodic effect.[46,47] Similar inhibition behavior has also been reported for other metals, such as copper and zinc, in chloride-containing media.[48] The BTA-based inhibitor forms a dense, hydrophobic film on the steel surface that restricts the penetration of aggressive species, thereby stabilizing the surface and inhibiting corrosion.[32]

As shown in Table 3, increasing the concentration of 1*H*-BTA leads to a significant reduction in corrosion current density (I_{corr}) and a corresponding increase in polarization resistance (R_p), likely due to enhanced adsorption of the BTA inhibitor on the steel surface.[28] Indeed, at a concentration of 2.5 mmol L^{-1}, the inhibitor demonstrates optimal performance, with I_{corr} reduced to 45.29 μA cm^{-2} and R_p increased to 1432 Ω cm^2. The highest inhibition efficiency (E%) achieved at this concentration is 74.13%.

Fig. 4b shows the potentiodynamic polarization curves recorded in the presence of different concentrations of CeO_2 NPs, up to 0.4%, under identical experimental conditions. Similar to the effect observed with 1*H*-BTA, increasing the concentration of CeO_2 NPs results in an anodic shift of the corrosion potential, particularly noticeable at 0.3% CeO_2 NPs, along with a decrease in both anodic and cathodic current densities, indicating a mixed-type inhibition mechanism with a dominant anodic component. This phenomenon is explained by the formation of a physical barrier layer, likely resulting from substrate oxidation accompanying the reduction of Ce^{4+} to Ce^{3+}, as outlined in reaction (6) and supported by Li et *al.*[49] In this case, the passivation mechanism of the CeO_2 film can be explained by the initial adsorption of CeO_2 particles onto the surface, followed by a redox process in which the passivating anion is reduced at defect sites within the oxide and hydroxide layers.[50]

$$2CeO_2 \rightleftarrows Ce_2O_3 + \frac{1}{2}O_2 \quad (6)$$

The corrosion current density decreases progressively with increasing CeO_2 NPs concentration, reaching a minimum value of 46.66 μA cm^{-2} at 0.3% CeO_2 NPs. This is accompanied by a corresponding increase in R_p, which reaches a maximum of 614 Ω cm^2 at the same concentration. However, beyond 0.3%, I_{corr} begins to increase while R_p decreases, suggesting that 0.3% is the optimal concentration for CeO_2 NPs as a corrosion inhibitor. The highest inhibition efficiency recorded at this concentration is 73.35%.

To enhance the corrosion resistance of carbon steel in a 3.5% NaCl solution, this study investigates the combined inhibition effect of the 1*H*-BTA and CeO_2 NPs. Fig. 4c presents the

Table 3 Electrochemical parameters obtained from potentiodynamic polarization curves of carbon steel in 3.5 wt% NaCl, showing the effects of 1*H*-BTA, CeO_2 NPs, and their combination system after 30 minutes of immersion[a]

	Electrochemical parameters					
Concentrations	E_{corr} (mV per AgCl)	I_{corr} (μA cm^{-2})	β_a (mV per dev.)	β_c (mV)	R_p (Ω cm^2)	E (%)
CeO_2NPs (wt%)						
Blank	−637	175.12	121.4	∞	301	—
0.1	−633	104.36	98.3	∞	409	40.40
0.2	−628	87.38	113.1	∞	562	50.10
0.3	−596	46.66	93.6	223.7	614	73.35
0.4	−629	102.18	99.2	∞	419	41.29
1*H*-BTA (mmol L^{-1})						
Blank	−637	175.12	121.4	∞	301	—
0.5	−604	80.85	159.0	∞	855	53.83
1.5	−577	48.56	145.2	∞	1300	72.27
2.5	−559	45.29	149.2	∞	1432	74.13
3.5	−528	49.58	143.8	∞	1261	71.68
1*H*-BTA + CeO_2NPs						
Blank	−637	175.12	121.4	∞	301	—
BTA (2.5 mmol L^{-1})	−559	45.29	149.2	∞	1432	74.13
CeO_2 (0.3%)	−596	46.66	93.6	223.7	614	73.35
BTA+0.05% CeO_2	−585	50.72	200.4	337.6	1140	71.03
BTA+0.10% CeO_2	−572	45.22	202.2	456.6	1346	74.17
BTA+0.15% CeO_2	−587	15.87	98.7	244.3	1923	90.93
BTA+0.20% CeO_2	−542	11.45	70.7	193.5	1964	93.46
BTA+0.25% CeO_2	−532	17.26	79.7	239.0	1504	90.14
BTA+0.30% CeO_2	−569	31.61	141.6	489.8	1508	81.95

[a] Values are reported as mean ± standard deviation (SD) based on 3–6 independent measurements.

potentiodynamic polarization curves obtained using the optimal concentration of 1*H*-BTA and varying CeO_2 NPs concentrations from 0.05% to 0.30%, along with a control sample without inhibitors.

As shown in Fig. 4c, the corrosion potential shifts toward more anodic values in the presence of 1*H*-BTA and increasing concentrations of CeO_2 NPs, compared to the uninhibited sample (blank). For CeO_2 NPs concentrations between 0.05% and 0.15%, the corrosion potential lies between those observed for 1*H*-BTA and CeO_2 NPs applied individually. As the CeO_2 concentration increases up to 0.25%, the corrosion potential shifts further in the anodic direction, indicating enhanced protection. However, at 0.30%, a slight decrease is observed, bringing the corrosion potential back to a level between those of the individual inhibitors. Additionally, a reduction in both anodic and cathodic current densities is observed, suggesting a mixed-type inhibition mechanism with predominantly anodic behavior. With increasing CeO_2 concentration in the presence of 1*H*-BTA, the corrosion current density (I_{corr}) shows a steady decline, reaching a minimum of 11.45 μA cm^{-2} at a concentration of 2.5 mmol per L 1*H*-BTA and 0.2% CeO_2.

This improvement is reflected in the polarization resistance (R_p), which attains a maximum value of 1964 Ω cm^2. Beyond the 0.2% CeO_2 threshold, however, I_{corr} begins to rise and R_p decreases, indicating a decline in protective performance. These results suggest that 2.5 mmol per L 1*H*-BTA combined with 0.2% CeO_2 represents the optimal concentration for the 1*H*-BTA–CeO_2 NPs system, achieving the highest recorded inhibition efficiency of 93.46%. BTA adsorbs onto the metallic surface, forming an initial protective layer. When combined with BTA, a CeO_2 NPs concentration of 0.2% exhibits a pronounced effect, significantly enhancing the stability of the anticorrosion protection.

Fig. 5 shows the Nyquist and Bode plots (EIS) of carbon steel after 30 minutes of immersion in a 3.5 wt% NaCl solution at room temperature, both without and with corrosion inhibitors (1*H*-BTA, CeO_2 NPs, and the 1*H*-BTA–CeO_2 NPs system). The corresponding EIS parameters, obtained through curve fitting with ZView software, are summarized in Table 4. To ensure reliable fitting of the EIS spectra, the error factor (χ^2) was constrained to values below 2.0×10^{-3}, validating the suitability of the employed equivalent circuit model. For comparison, the EIS response of the blank sample is also included. The equivalent circuits used to model the EIS data are illustrated in Fig. 5a, c, and e, corresponding to the 1*H*-BTA, CeO_2 NPs, and 1*H*-BTA–CeO_2 NPs system, respectively. In the equivalent circuit models, R_s, R_c, and R_{ct} denote the solution resistance, the resistance of the outer layer, and the charge-transfer resistance at the electrode/electrolyte interface, respectively. The constant phase elements, CPE_c and CPE_{dl}, account for the non-ideal capacitive behavior of the outer layer and the double layer, respectively, with the exponent n reflecting deviations from ideality and

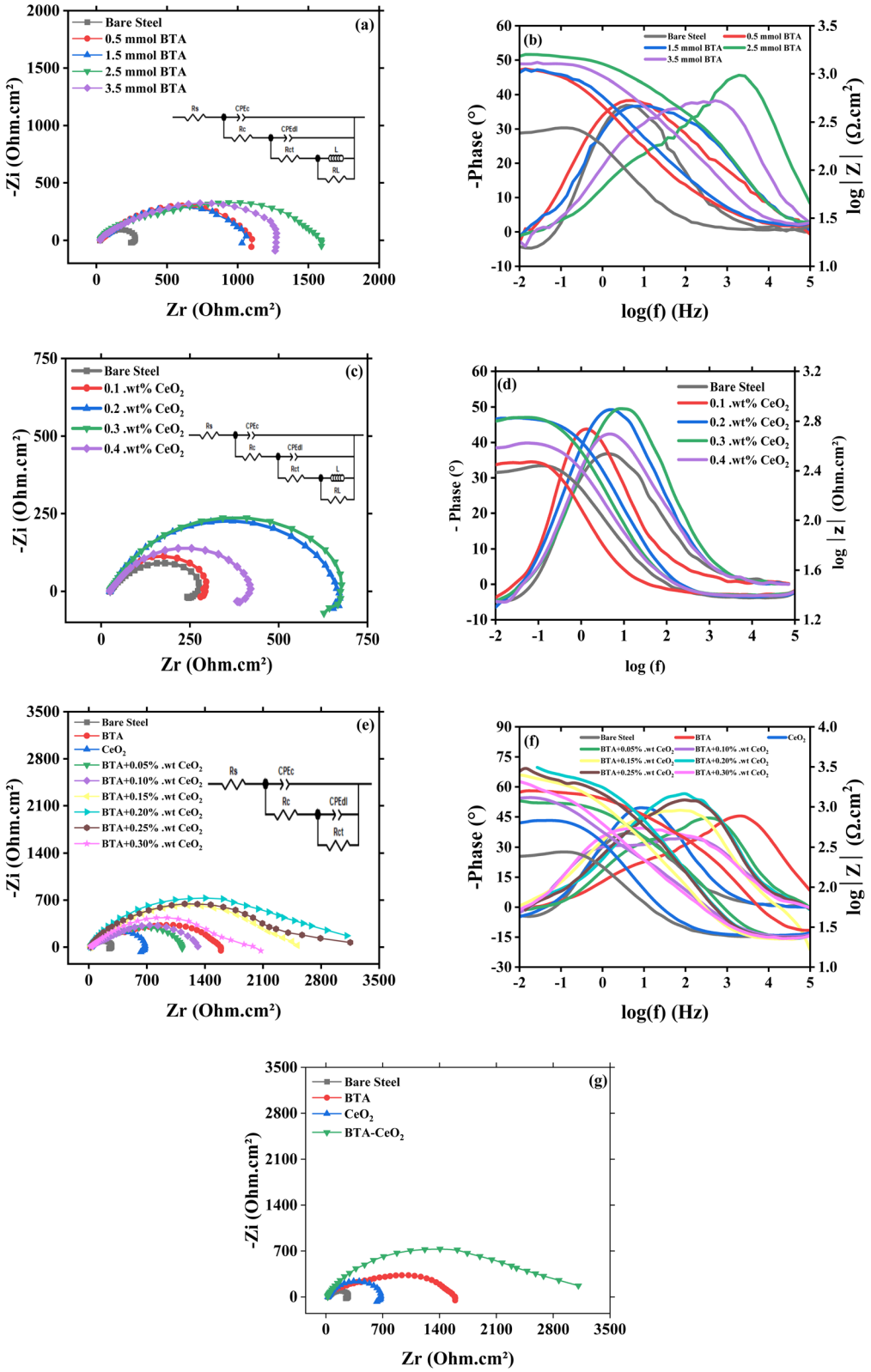

Fig. 5 Nyquist and Bode plots of carbon steel in 3.5 wt% NaCl at room temperature, showing the effects of: (a and b) increasing 1*H*-BTA concentrations; (c and d) increasing CeO_2 NPs concentrations; (e and f) varying CeO_2 NPs concentrations at the optimal 1*H*-BTA concentration; and (g) comparing optimal concentrations of 1*H*-BTA, CeO_2 NPs, and their composite after 30 min immersion.

Table 4 Electrochemical parameters from EIS measurements of carbon steel in 3.5 wt% NaCl, as a function of 1*H*-BTA concentration, CeO_2 NPs concentration, and their combination system after 30 min immersion[a]

	Electrochemical parameters									
Concentrations	R_S (Ω cm^2)	CPE_C (F s$^{(n-1)}$)	n_c	R_c (Ω cm^2	CPE_{dl} (F s$^{(n-1)}$)	n_{ct}	R_{ct} (Ω cm^2)	C_{eff} (μF cm^{-2})	E (%)	X^2
CeO_2NPs (wt%)										
Blank	23.86	0.0007764	0.73	105.1	0.000473	0.87	174.0	238	—	0.00169
0.1	25.46	0.0007815	0.85	21.9	0.000921	0.86	267.3	235	34.90	0.00127
0.2	24.38	0.0001644	0.85	68.9	0.000214	0.71	584.7	57.2	70.24	0.00065
0.3	24.96	0.0002348	0.84	53.4	0.000396	0.73	632.9	89.1	72.50	0.00087
0.4	24.71	0.0003137	0.81	60.5	0.000399	0.79	345.4	120	49.62	0.00138
1*H*-BTA (mmol L^{-1})										
Blank	23.86	0.0007764	0.73	105.1	0.000473	0.87	174.0	238	—	0.00169
0.5	25.52	0.0001671	0.65	63.42	0.000359	0.63	1070	88.9	83.73	0.00276
1.5	25.95	0.0001790	0.64	191.4	0.000216	0.69	901.7	163	80.70	0.00137
2.5	25.62	0.0000647	0.77	334.1	0.000144	0.53	1292	28.4	86.53	0.00039
3.5	26.47	0.0001904	0.77	150.6	0.000195	0.54	1263	48.6	86.22	0.00063
1*H*-BTA + CeO_2NPs										
Blank	23.86	0.0007764	0.73	105.1	0.000473	0.87	174.0	238	—	0.00169
BTA (2.5 mmol L^{-1})	25.62	0.0000647	0.77	334.1	0.000144	0.53	1292	28.4	86.53	0.00039
CeO_2 (0.3%)	24.96	0.0002348	0.84	53.4	0.000396	0.73	632.9	89.1	72.50	0.00087
BTA+0.05% CeO_2	23.06	0.0000234	0.80	254.5	0.000179	0.66	881.6	54.6	80.26	0.00045
BTA+0.10% CeO_2	22.63	0.0001773	0.64	300.8	0.000509	0.73	998.4	90.6	82.57	0.00301
BTA+0.15% CeO_2	22.25	0.0000386	0.83	195.3	0.000202	0.58	2176	21.6	92.00	0.00083
BTA+0.20% CeO_2	23.16	0.0000049	0.98	19.79	0.000085	0.60	2591	11.6	93.28	0.00079
BTA+0.25% CeO_2	22.80	0.0000258	0.83	287.9	0.000151	0.51	2315	04.2	92.48	0.00138
BTA+0.30% CeO_2	22.44	0.0001098	0.71	147.7	0.000326	0.63	1619	44.9	89.13	0.00545

[a] Values are reported as mean ± standard deviation (SD) based on 3–6 independent measurements.

providing insight into surface roughness or inhomogeneity.[51] The inductive elements, L and R_L, represent the inductance and its associated resistance, capturing the inductive loop features observed in the EIS spectra. This loop, typically observed at low frequencies, is attributed to surface reaction dynamics or to system instabilities.[52]

Because the CPE_{dl} values derived from the impedance curves are unrealistically high and beyond the standard range, an effective capacitance (C_{eff}) was introduced to more accurately describe the actual capacitance related to the measured impedance (see Table 4). The C_{eff} values were determined according to the following equation:

$$C_{eff} = \left[CPE_{dl} \left(\frac{1}{R_s} + \frac{1}{R_{ct}} \right)^{n-1} \right]^{\frac{1}{n}} \quad (7)$$

The inhibition efficiency was also determined from the EIS measurements using the eqn (8).[53] Here, $R_{ct(0)}$ denotes the charge transfer resistance without the corrosion inhibitor, while $R_{ct(i)}$ refers to the resistance in its presence.

$$E\% = \frac{R_{ct(0)} - R_{ct(i)}}{R_{ct(0)}} \quad (8)$$

The Nyquist diagrams recorded in the absence and presence of 1*H*-BTA and CeO_2 NPs inhibitors (see Fig. 5a and c) exhibit a characteristic semicircular arcs, suggesting that corrosion kinetics are controlled by charge-transfer resistance and that the overall corrosion mechanism remains essentially unchanged by inhibitor addition compared with the blank sample. These arcs are not perfect semicircles due to frequency dispersion, which results from surface roughness and electrode non-uniformities.[54] The depressed shape of the each arc reflects the presence of two distinct time constants at high and mid frequencies (HF and MF). The HF response is typically associated with the accumulation of corrosion products, whereas the MF response is attributed to charge–transfer processes at the electrode/electrolyte interface.[55]

At low frequencies (LF), a pronounced inductive loop emerges. Although its origin is not fully resolved, it has been widely ascribed to adsorption/relaxation effects, passive layer dynamics, and/or redox processes.[56,57]

For the blank sample, the inductive loop is likely associated with the adsorption of Cl^- and Fe^{2+} species on the carbon steel surface. In the presence of 1*H*-BTA and CeO_2 NPs inhibitors, this loop persists, indicating that the inhibitor-derived films do not completely prevent the penetration of Cl^- and Fe^{2+} ions to the carbon steel surface.[41] In contrast, under the combination conditions, as shown in Fig. 5e, the inductive loop at LF disappears. This behavior indicates that the composite film effectively suppresses the ingress of aggressive ions, thereby enhancing film stability and improving corrosion resistance.[41]

Additionally, an increase in the semicircular arc diameter is observed with increasing inhibitor concentration, reaching up to 2.5 mmol L^{-1} for 1*H*-BTA and 0.3% for CeO_2 NPs, corresponding to inhibition efficiencies of 86.53% and 72.50%, respectively. Under the combination conditions, the highest efficiency of approximately 93.28% was achieved with the combination of 2.5 mmol L^{-1} 1*H*-BTA and 0.20% CeO_2 (see Table 4).

This improvement reflects a significant increase in charge-transfer resistance (R_{ct}) and decrease in effective capacitance (C_{eff}), consistent with the formation of a stable adsorbed film on the carbon steel surface that provides effective protection against corrosion. However, when the concentrations of 1*H*-BTA, CeO_2 NPs, and the 1*H*-BTA–CeO_2 NPs system exceed their optimal ranges, the R_{ct} values begin to decrease, corroborating the polarization test results that established the most effective inhibitor levels. Moreover, the Bode plots (Fig. 5b, d, and f) reveal that the phase angle shifts to more negative values in the presence of inhibitors compared to the blank sample. This shift becomes more pronounced with increasing inhibitor concentration and is accompanied by a rise in the impedance modulus, indicating a more resistive system.

Furthermore, Fig. 5g shows the Nyquist plots recorded after 30 minutes of immersion in a 3.5 wt% NaCl solution at room temperature, both in the absence and in the presence of the optimal concentrations of 1*H*-BTA, CeO_2 NPs, and the 1*H*-BTA–CeO_2 NPs hybrid system. For comparison, the highest corrosion inhibition efficiency for carbon steel in 3.5 wt% NaCl solution was achieved through the synergistic effect of the 1*H*-BTA–CeO_2 NPs hybrid system. Notably, the charge transfer resistance (R_{ct}) of this hybrid system is twice that observed with 1*H*-BTA alone, and four times higher than with CeO_2 NPs. For the results obtained by electrochemical techniques, the efficiencies determined by polarization are very close to those obtained by impedance (EIS), confirming the consistency and reliability of the results.

The synergy index (S.I.) can be calculated using the approach by Aramaki and Hackerman (eqn (9)):[58]

$$S.I = \frac{1 - \eta_{BTA+Ce}}{1 - \eta_{BTA} - \eta_{Ce} + \eta_{BTA}\eta_{Ce}} \quad (9)$$

where: η_{CeO_2} = inhibition efficiency of CeO_2 alone (73.35%)

η_{BTA} = inhibition efficiency of Ce^{3+} alone (85.10%)

$\eta_{BTA+CeO_2}$ = inhibition efficiency of hybrid system (93.46%)

Using the inhibition efficiencies determined from polarization measurements (η_{BTA} =73.35, η_{CeO_2} = 85.10, $\eta_{BTA+CeO_2}$= 93.46, the synergy index S.I is found to be 1.65.

A synergy index greater than unity confirms genuine synergistic interaction between BTA and the cerium-based inhibitors. This synergy arises from complementary mechanisms: BTA provides anodic protection through chelation with Fe^{2+}/Fe^{3+} ions, while CeO_2/Ce^{3+} provides cathodic protection through the formation of insoluble cerium hydroxides/oxides. The resulting mixed film (Fe-BTA-CeO_2) exhibits enhanced barrier properties, as confirmed by the increased Rct values in EIS measurements.[33,59]

3.1.2. Morphology and characterization of the steel surfaces. SEM imaging was carried out to examine the interactions between the inhibitors and the carbon steel surface after 30 minutes of immersion in 3.5% NaCl solution at room temperature. Fig. 6a–d shows the surface morphologies of four specimens: (a) immersed in 3.5% NaCl without inhibitor, (b) with 0.3% CeO_2 NPs, (c) with 2.5 mmol L^{-1} 1*H*-BTA, and (d) with a combination of 2.5 mmol L^{-1} 1*H*-BTA and 0.2% CeO_2 NPs. Fig. 6e and f present the corresponding elemental EDX maps for the specimens treated with CeO_2 NPs alone and with the 1*H*-BTA–CeO_2 NPs composite, respectively. The atomic percentages of C, O, N, and Ce, determined from surface mapping using EDS analysis (Fig. 7), are summarized in Table 5 for each of the four films. In the uninhibited specimen (blank) (Fig. 6a), the surface is covered with corrosion products and exhibits severe damage due to the aggressive attack of chloride ions, leading to crack formation and resulting in a heterogeneous, rough morphology. In contrast, the CeO_2 inhibited sample (Fig. 6b) exhibits a more uniform, continuous layer across the entire substrate, with only a few scattered cracks. The detection of Ce (Table 5) suggests an improvement in the film protective quality. When 1*H*-BTA is present (Fig. 6c), the resulting film appears relatively homogeneous, featuring some cracks and the emergence of worm-like patterns across the entire surface, indicative of 1*H*-BTA adsorption. EDS analysis (Fig. 7 & Table 5) reveals a new peak corresponding to nitrogen (N), providing strong evidence for the presence of BTA molecules.[60] In non-corroded regions (crack-free), BTA reacts with Fe to form a protective layer, whereas in corroded areas (exhibiting cracks), BTA complexes with Fe^{2+} and the resulting complex deposits within corrosion pits, effectively blocking further attack.[38] In the presence of corrosion products such as Fe^{2+}, BTA molecules can interact with these ions, leading to the formation of an organometallic complex of the type [Fe(BTA)].[61] The resulting layer can organize into a three-dimensional polymeric network, denoted as $[Fe_n(\text{-BTA})_p]_m$, forming a dense, hydrophobic, and protective barrier commonly referred to as an organometallic film.[62] Moreover, BTA contributes to the stabilization of corrosion products such as FeOOH by adsorbing onto their surfaces.[33] This adsorption promotes the formation and maintenance of the passive layer, limiting the access of corrosive species to the metal surface.[63]

In the presence of BTA, spontaneously formed corrosion products become more resistant to degradation. BTA thus acts as a defect blocker, reducing the porosity of the layer and slowing down oxide dissolution. The overall effect is a decrease in the solubility of the passivation layer, which becomes thinner, more homogeneous, and more stable, without the formation of an additional thick organometallic layer.

The surface treated with the 1*H*-BTA–CeO_2 NPs system (Fig. 6d) appears more homogeneous, crack-free, and shows no visible signs of corrosion. This treatment also increases the Ce and N contents in the film, confirming the strong barrier effect of the hybrid system. The elevated Ce and N levels indicate that CeO_2 NPs from the hybrid system migrated to the scratched regions, where the loaded BTA molecules were successfully released.[37]

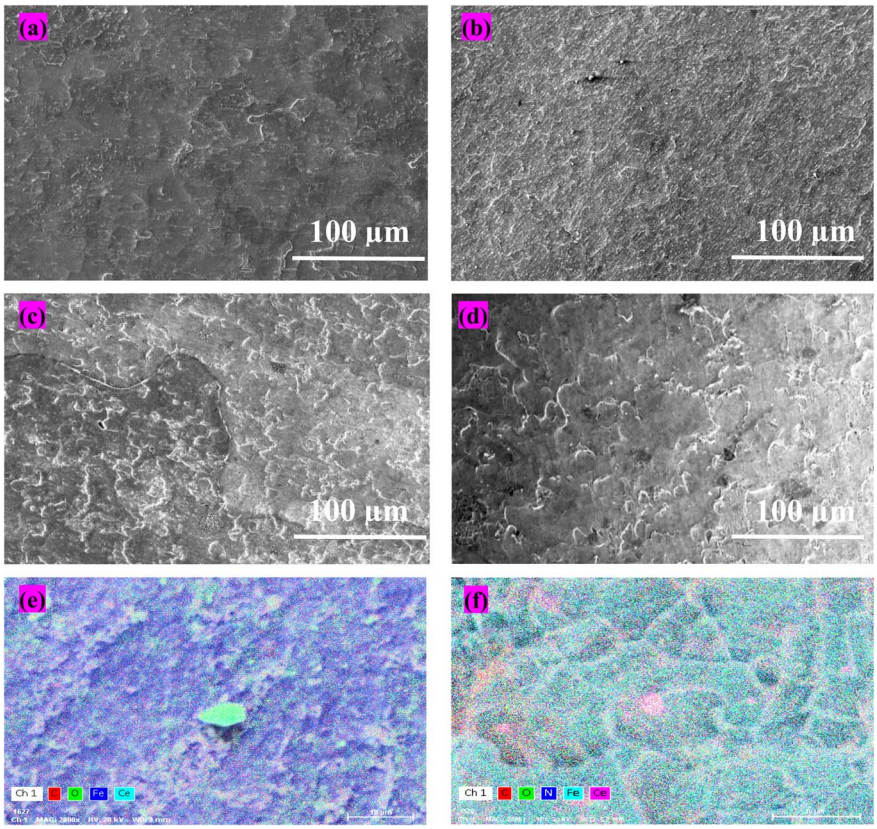

Fig. 6 Scanning electronic microscopy (SEM) surface morphologies of carbon steel after 30 minutes of immersion in 3.5% NaCl at room temperature: (a) bare steel (blank), (b) with CeO_2 NPs, (c) with 1*H*-BTA, and (d) with a 1*H*-BTA–CeO_2 NPs hybrid system. Elemental surface EDS maps are shown in (e) and (f) for CeO_2 NPs and the 1*H*-BTA–CeO_2 NPs hybrid system, respectively.

3.2. Influence of immersion time on the corrosion inhibition performance

3.2.1. Electrochemical behavior. In this part, the aim is to determine the effect of the inhibition films on the corrosion resistance of carbon steel surfaces at different immersion times. The corrosion inhibition of carbon steel was evaluated both in the absence (blank) and in the presence of inhibitors (1*H*-BTA, CeO_2 NPs, and the 1*H*-BTA–CeO_2 NPs hybrid system) at their optimal concentrations during prolonged immersion (up to 14 days) in a 3.5 wt% NaCl solution at room temperature. Electrochemical impedance spectroscopy (EIS) was employed for this purpose. The EIS diagrams obtained with and without inhibitors (blank) are shown in Fig. 8, while the corresponding electrochemical parameters recorded over 0–14 days are summarized in Table 6. The equivalent electrical circuits used to model the impedance responses are also presented in Fig. 8.

Fig. 8a and b illustrates the evolution of Nyquist and Bode plots for a carbon steel electrode (blank) immersed in 3.5 wt% NaCl solution at room temperature for up to 14 days. The shape of the curves clearly reveals two distinct relaxation times: the first, at high frequencies, is attributed to the resistance of the corrosion product film (R_c), while the second, at medium frequencies, corresponds to the charge transfer resistance (R_{ct}).[64] The quantitative data are summarized in Table 6. A pronounced increase in R_{ct} is observed after the first day of immersion, indicating the initial development of a passive film on the carbon steel surface. With prolonged exposure, however, R_{ct} gradually decreases, reflecting the progressive degradation of the surface in the corrosive environment. Beyond 7 days, R_{ct} tends to stabilize, suggesting that the corrosion products formed on the steel surface provide a self-protective effect. The Bode plots further show a decrease in the maximum phase angle at medium frequencies and a shift toward lower frequencies, highlighting a marked reduction in capacitive behavior.

Fig. 8c–h presents the EIS diagrams (Nyquist and Bode) for carbon steel immersed for up to 14 days in a 3.5 wt% NaCl solution containing 1*H*-BTA, CeO_2 NPs, and the combined 1*H*-BTA–CeO_2 NPs inhibitors at their optimal concentrations. The proposed equivalent circuits are shown in Fig. 8c, e, and h, and the corresponding fitting results are summarized in Table 6. In all cases, the impedance spectra exhibit two distinct time constants: one at high frequencies, attributed to the film resistance, and another at mid-to-low frequencies, corresponding to the charge transfer resistance (R_{ct}). As reported in Table 6 and illustrated in Fig. 9, the R_{ct} values initially decrease during the first day of immersion but subsequently increase and stabilize up to 14 days for all inhibitors. This rise and stabilization of R_{ct} can be attributed to the self-healing effect of corrosion products formed on the steel surface, together with the protective films, which effectively hinder both ionic and electronic transport across the layer.

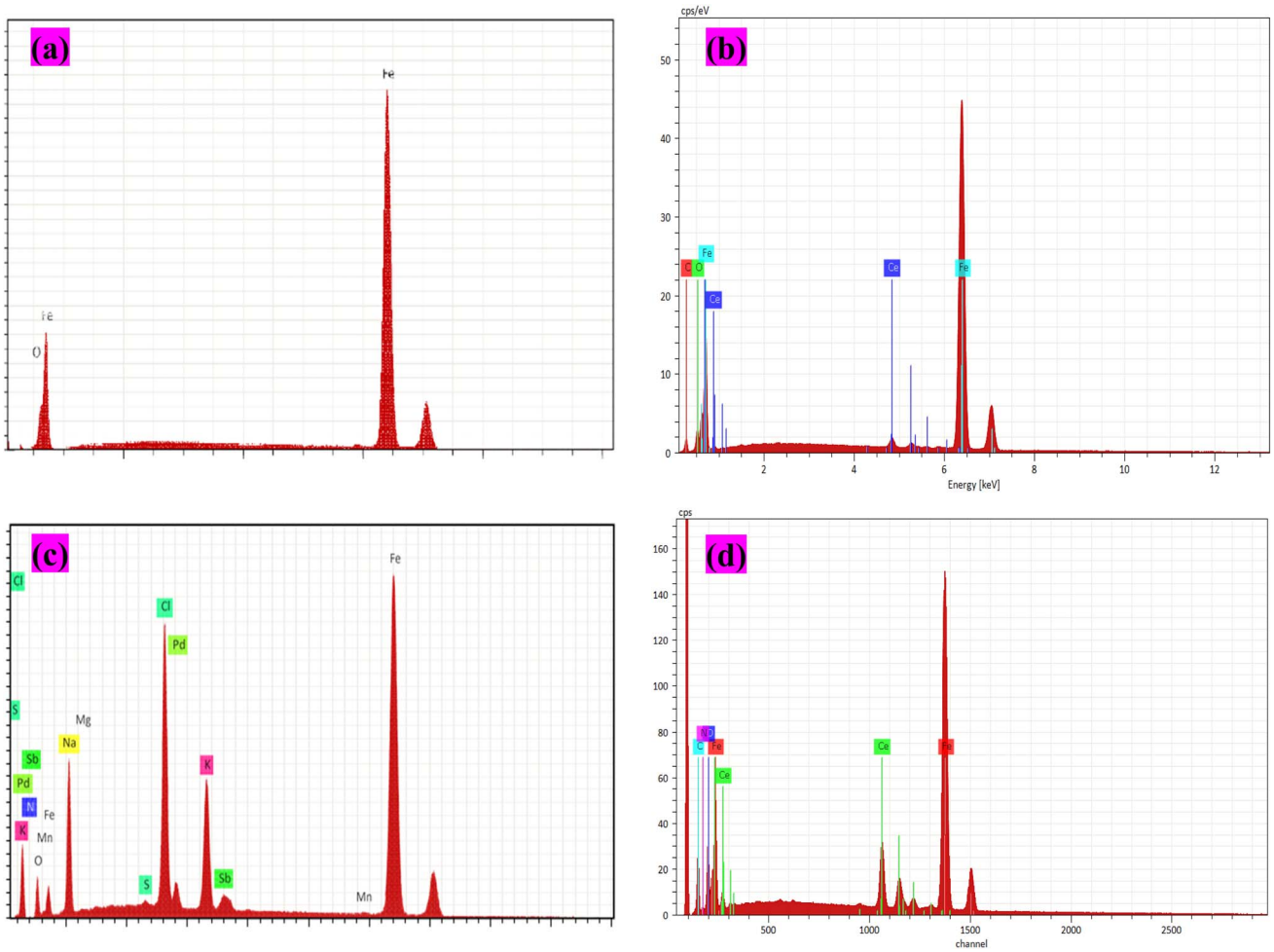

Fig. 7 Energy-dispersive spectroscopy (EDS) spectra of carbon steel after 30 minutes of immersion in 3.5% NaCl at room temperature: (a) bare steel (blank), (b) with CeO_2 NPs, (c) with 1*H*-BTA, and (d) with a 1*H*-BTA–CeO_2 NPs hybrid system.

For the 1*H*-BTA and 1*H*-BTA–CeO_2 NPs inhibitors, an additional element associated with diffusion resistance (W) appears in the equivalent circuit after 2 and 14 days of immersion, respectively. This element is represented by an open-circuit finite-length Warburg impedance (Fig. 8c and g). In general, Warburg-type diffusive behavior is likely linked to the wettability and porosity of the film, which promote the penetration of aggressive species such as chloride ions (Cl^-) and oxygen (O_2) to the interface. This penetration compromises the stability of the system and accelerates its degradation.[65]

Table 5 Average surface elemental composition (at%), rounded to the nearest integer, derived from EDS mapping after 30 minutes of immersion in 3.5% NaCl at room temperature

Elements	Fe substrate	CeO_2 NPs	1*H*-BTA	1*H*-BTA–CeO_2 NPs
Fe	Balance	Balance	Balance	Balance
C	3.41	2.21	2.55	2.75
O	3.70	1.80	4.10	5.14
N	—	—	0.48	0.67
Ce	—	3.07	—	18.10

The incorporation of CeO_2 NPs in combination with 1*H*-BTA layer markedly improves the quality of the protective film, even after prolonged immersion. As shown in Table 6 and Fig. 9, the charge transfer resistance (R_{ct}) values are significantly higher than those obtained with 1*H*-BTA or CeO_2 alone, clearly demonstrating the improved corrosion protection provided by the 1*H*-BTA–CeO_2 system. After 14 days of immersion, the inhibition efficiency (E%) of the composite reaches 92.90%, compared to 85.56% and 45.09% for 1*H*-BTA and CeO_2, respectively. In addition, the R_{ct} value of the 1*H*-BTA–CeO_2 NPs system (Fig. 8i) is approximately twice that of BTA alone and nearly eight times greater than that of CeO_2 alone.

Overall, the combined inhibition effect of 1*H*-BTA and CeO_2 NPs ensures superior protection: BTA adsorbs onto and blocks the active corrosion sites, while CeO_2 nanoparticles reinforce this effect by stabilizing and strengthening the inhibitor film.

3.2.2. Morphology and characterization of the steel surfaces

3.2.2.1. Optical microscope. Optical microscopy (OM) observations of the carbon steel surface after 14 days of immersion in a 3.5% NaCl solution, in the absence and

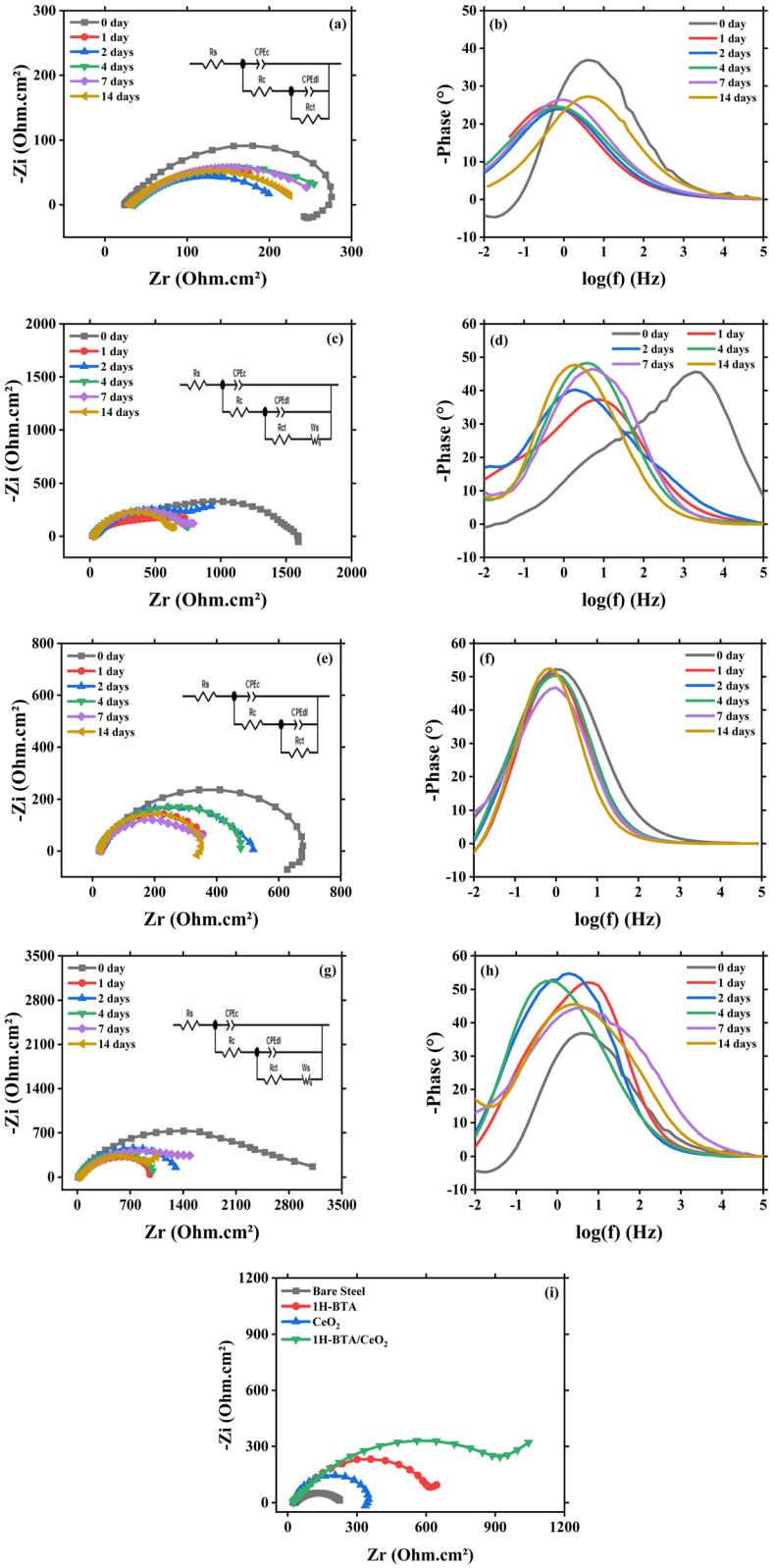

Fig. 8 Nyquist and Bode plots of carbon steel in 3.5 wt% NaCl solution at room temperature as a function of immersion time (up to 14 days): (a and b) bare carbon steel (blank), (c and d) with 1*H*-BTA inhibitor, (e and f) with CeO_2 NPs inhibitor, (g and h) with 1*H*-BTA/CeO_2 NPs hybrid system, and (i) comparison of 1*H*-BTA, CeO_2 NPs, and the hybrid system after 14 days of immersion.

Table 6 Fitting results of EIS data for bare carbon steel (blank), and samples with 1*H*-BTA, CeO_2 NPs and 1*H*-BTA–CeO_2 NPs inhibitors in 3.5 wt% NaCl solution, as a function of immersion time up to 14 days[a]

	Electrochemical parameters									
Time of immersion	R_S (Ω cm^2)	CPE_C (F cm^{-2} s$^{(1-n)}$)	n_C	R_C (Ω cm^2)	CPE_{dl} (F cm^{-2} s $^{(1-n)}$)	n_{dl}	R_{Ct} (Ω cm^2)	C_{eff} (μF cm^{-2})	E (%)	X^2
Bare steel (blank)										
0 day	23.86	0.000776	0.73	105.1	0.000473	0.87	174.0	238	—	0.00169
1 day	26.03	0.000176	0.42	18.4	0.006318	0.57	207.7	1960	—	0.00010
2 days	23.10	0.005771	0.54	01.2	0.005711	0.57	181.1	1520	—	0.00011
4 days	25.78	0.002076	0.47	01.23	0.004984	0.54	174.9	1100	—	0.00041
7 days	22.54	0.004437	0.57	166.6	0.000661	0.83	73.82	800	—	0.00056
14 days	19.02	0.001984	0.59	131.8	0.000207	0.57	75.88	2070	—	0.00017
1*H*-BTA										
0 day	25.62	0.0000647	0.77	334.1	0.000144	0.53	1292	28.4	86.53	0.00039
1 day	26.91	0.0007785	0.64	394.8	0.000150	0.50	640.2	58.0	67.55	0.00020
2 days	26.10	0.0009620	0.56	141.9	0.000174	0.83	881.4	209	79.45	0.00054
4 days	25.63	0.0004074	0.79	17.98	0.000359	0.62	755.2	476	76.84	0.00067
7 days	25.88	0.0001844	0.88	65.21	0.000586	0.63	739.3	780	90.01	0.00079
14 days	27.65	0.0006454	0.81	104.6	0.000466	0.80	525.6	869	85.56	0.00082
CeO_2NPs										
0 day	24.96	0.0002348	0.84	53.43	0.000396	0.73	632.9	89.1	72.50	0.00087
1 day	24.68	0.0020836	0.92	186.4	0.002602	0.88	163.0	1230	—	0.00249
2 days	24.40	0.0017687	0.91	148.8	0.002004	0.73	317.0	1150	42.87	0.00397
4 days	24.10	0.002012	0.89	238.7	0.004096	0.88	220.6	1610	20.71	0.00429
7 days	23.73	0.001649	0.96	21.29	0.002384	0.56	349.1	1180	78.85	0.00423
14 days	25.95	0.002692	0.93	196.6	0.002626	0.85	138.2	1560	45.09	0.00181
1*H*-BTA + CeO_2NPs										
0 day	23.16	0.000049	0.98	19.79	0.000085	0.60	2591	7.0	93.28	0.00079
1 day	22.79	0.000429	0.86	314.40	0.000126	0.71	716	11.6	70.99	0.00069
2 days	21.86	0.000721	0.86	215.90	0.000812	0.66	1176	11.0	84.60	0.00195
4 days	21.93	0.000106	0.79	89.16	0.000774	0.80	974.7	72.3	82.05	0.00188
7 days	22.11	0.000123	0.81	37.57	0.000636	0.56	1646	177.0	95.51	0.00055
14 days	24.21	0.000239	0.81	52.72	0.000684	0.63	1069	89.8	92.90	0.00042

[a] Values are reported as mean ± standard deviation (SD) based on 3–6 independent measurements.

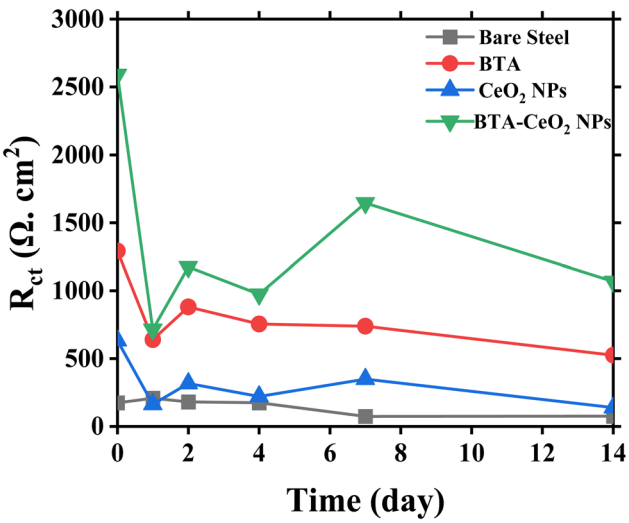

Fig. 9 Evolution of charge transfer resistance (R_{ct}) as a function of immersion time in 3.5 wt% NaCl solution for bare carbon steel (blank) and for samples with 1*H*-BTA, CeO_2 NPs, and 1*H*-BTA–CeO_2 NPs inhibitors over 14 days.

presence of CeO_2 NPs, 1*H*-BTA, and 1*H*-BTA–CeO_2 NPs inhibitors, are presented in Fig. 10. As shown in Fig. 10a, the surface exhibits a heterogeneous appearance, with numerous pores, pits, and dark regions, indicating significant corrosion activity induced by the chloride ions. In contrast, the presence of the inhibitors (Fig. 10b–d) results in less heterogeneous surface films. Among them, the surface treated with the combined 1*H*-BTA–CeO_2 NPs inhibitor displays the most uniform, with thinly layer formed, suggesting improved protective film formation compared to the individual inhibitors.

3.2.2.2. XRD analysis. The X-ray diffraction (XRD) patterns of carbon steel after 14 days of immersion in a 3.5% NaCl solution, in the absence and presence of inhibitors (CeO_2 NPs, 1*H*-BTA, and 1*H*-BTA–CeO_2 NPs), are presented in Fig. 11. The diffraction patterns reveal the characteristic peaks of the iron substrate (Fe), together with additional reflections corresponding to corrosion products and inhibitor-related compounds. The presence of BTA is associated with the formation of Fe–BTA complexes, which are typically amorphous or poorly crystalline, as evidenced by a slight increase in

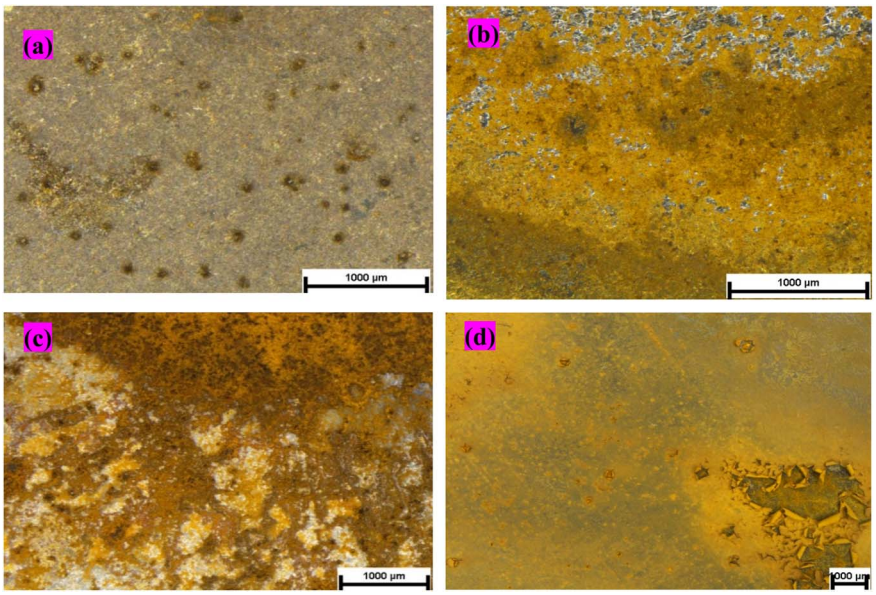

Fig. 10 Optical microscope images of carbon steel after 14 days in 3.5% NaCl at room temperature: (a) without inhibitor (blank), (b) with CeO_2 NPs, (c) 1*H*-BTA, and (d) 1*H*-BTA–CeO_2 NPs inhibitors.

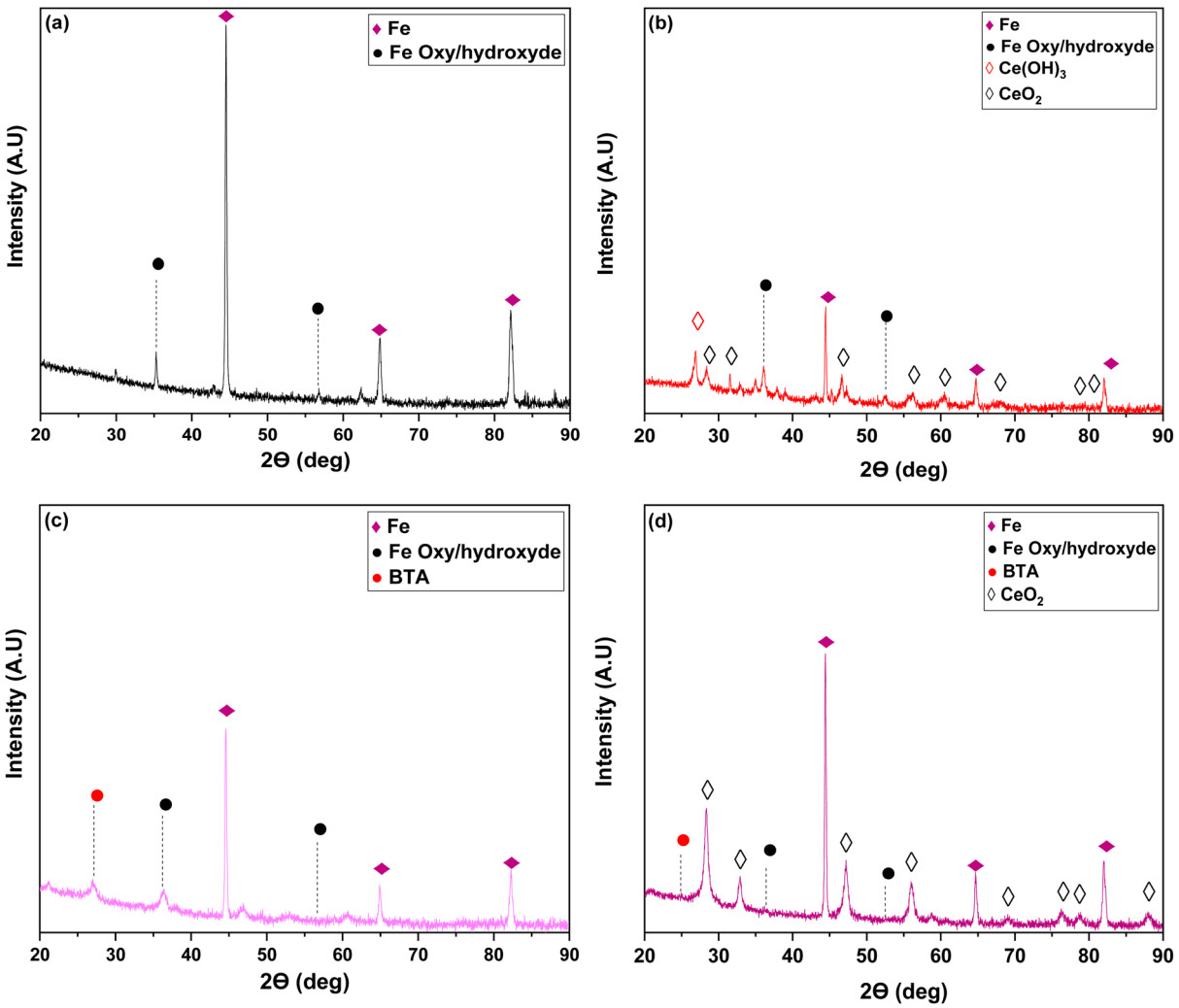

Fig. 11 X-ray diffraction (XRD) patterns of carbon steel surfaces after 14 days of immersion in 3.5% NaCl solution: (a) bare carbon steel (blank), (b) with CeO_2 NPs, (c) with 1*H*-BTA, and (d) with 1*H*-BTA–CeO_2 NPs inhibitors.

background amorphization. The detection of crystalline CeO_2 with a fluorite structure confirms that the cerium nanoparticles remain on the steel surface even after prolonged immersion.

The increased intensity of Fe and Fe oxide/hydroxide peaks observed in the hybrid system, compared to 1*H*-BTA alone, is more likely associated with the stabilization and retention of corrosion products rather than with an acceleration of the corrosion process.[66] In the presence of 1*H*-BTA alone, the inhibitor adsorbs onto the metal surface and forms complexes with Fe^{2+} ions, thereby reducing metal dissolution and promoting the formation of a protective film.[67] Nevertheless, oxide and hydroxide species can still develop, albeit in a more controlled and stabilized manner.[67]

In the 1*H*-BTA–CeO_2 NPs hybrid system, BTA is able to interact with both the metal substrate and the CeO_2 NPs. This dual interaction may reduce its exclusive coordination with Fe^{2+} ions, allowing the formation and accumulation of iron oxide/hydroxide species that become incorporated and stabilized within the protective layer.[39] Consequently, the higher detected intensity of corrosion product peaks does not necessarily indicate increased degradation, but rather improved retention within the film.

Furthermore, the persistence of CeO_2 NPs at the film surface, even after prolonged immersion, highlights their active role in the protection mechanism. Owing to the reversible Ce^{4+}/Ce^{3+} redox couple and the presence of oxygen vacancies, CeO_2 can participate in interfacial redox processes. Upon partial degradation of the protective layer, these defect sites may facilitate electron transfer and promote the re-adsorption of BTA molecules. This behavior supports a dynamic re-passivation mechanism, contributing to the regeneration of a more stable and protective surface layer that effectively limits the ingress of aggressive species.[39,68]

As demonstrated in coating-based systems reported in ref. 38 and 39, the inhibition process relies on the slow diffusion of BTA through the coating matrix, where its release is governed by pH-triggered mechanisms or gradual migration toward the metal/coating interface. In such systems, CeO_2 primarily functions as a physical barrier. In contrast, in the present study, both BTA and CeO_2 NPs are directly available at the steel/electrolyte interface without any transport limitations imposed by a coating matrix, enabling immediate interfacial interactions and the rapid formation of a protective film. BTA adsorption occurs within minutes, while Ce^{3+} released from CeO_2 provides immediate supplementary inhibition. This enables a fundamentally different inhibition mechanism characterized by rapid synergistic protection, in contrast to the long-term self-healing and controlled-release mechanisms typically associated with coating-based systems. Based on a comparison between previous works[38,39,63] and the findings of this study, it can be concluded that in coating systems, the corrosion inhibition process involves.

- Matter transport: BTA must first diffuse through the polymer matrix[39] or be released from containers before reaching the steel surface

- Time-dependent availability: BTA concentration at the metal/coating interface builds up slowly

- pH-activation: in paper,[38] BTA release is specifically triggered by local pH changes at corrosion sites.

- CeO_2 as container: the oxide serves primarily as a physical reservoir, with Ce^{3+} release as a secondary benefit

However, in solution systems (in this work) the process involves.

- Instant availability: both BTA and CeO_2 are directly accessible to the steel surface

- Competitive/cooperative adsorption: BTA and Ce^{3+}/CeO_2 simultaneously interact with the surface

- Rapid film formation: protective layers form within minutes

- CeO_2 as active inhibitor: nanoparticles directly participate in inhibition, not just as containers

A schematic representation of the proposed corrosion inhibition mechanism of the 1*H*-BTA–CeO_2 NP system on the steel surface in 3.5% NaCl solution is presented in Fig. 12.

Thus, as a partial conclusion highlighting the superior protective performance of the CeO_2/1*H*-BTA system introduced into the solution, Table 7 summarizes selected previous studies reporting the corrosion inhibition efficiencies of CeO_2, BTA, and CeO_2/BTA systems and compares them with the results obtained in the present work. Various interaction mechanisms between these inhibitors and metal surfaces have been reported, resulting in different levels of corrosion protection efficiency.

Previous studies have shown that the inhibition mechanism of BTA on steel surfaces has been attributed to adsorption, leading to the formation of strong BTA–Fe interactions and the development of a protective adsorbed layer such as $[Fe_n(BTA)_m]$ and $[Fe_n(Cl)_p(BTA)_m]$, which effectively suppress corrosion activity.[35,69,70] Furthermore, the combination of BTA with other corrosion inhibitors, such as Na_2HPO_4 or cobalt species, has been shown to improve corrosion resistance through synergistic effects. In these systems, protection is generally attributed to the formation of compact protective films composed of Fe–BTA complexes and iron phosphates,[71] or to the precipitation of a BTA–Co chelate layer on the steel surface.[72] Based on the experimental results obtained in this study, BTA molecules strongly interact with the steel surface through the formation of Fe–BTA complexes, generating a protective adsorbed film. Simultaneously, CeO_2 nanoparticles act as physical barriers by occupying surface defects, pores, and damaged regions of the protective layer, thereby enhancing its compactness and stability. This combination effect results in a highly efficient protective film, providing a corrosion inhibition efficiency of approximately 93.4%.

3.3. Adsorption isotherms and thermodynamic parameters

To gain deeper insight into the interaction mechanisms between corrosion inhibitors and metal surface, various adsorption processes were considered. Several adsorption isotherm models, including Langmuir, Temkin, and Frumkin, which are extensively reported in the literature, were evaluated to determine the model that best describes the experimental data. During the corrosion inhibition process, inhibitor molecules undergo continuous adsorption and desorption at the

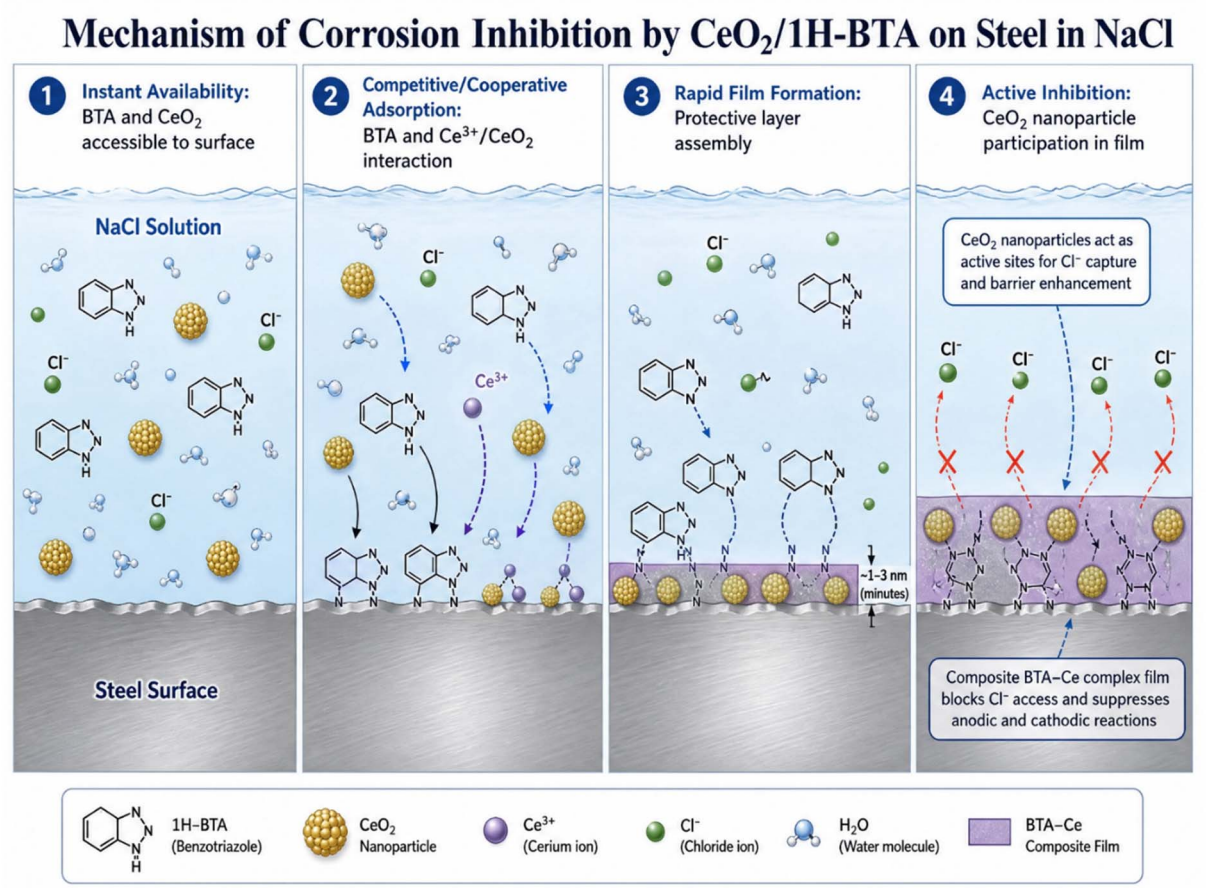

Fig. 12 Proposed corrosion inhibition mechanism of the 1*H*-BTA–CeO_2 NP system on the steel surface in 3.5% NaCl solution.

metal/solution interface until a quasi-equilibrium state is established. Analyzing this equilibrium behavior through appropriate adsorption isotherm models provides valuable information on the nature and strength of the interactions between the inhibitor species and the metal surface.

According to the Langmuir adsorption isotherm,[73] the adsorbed species form a monolayer on the metal surface. This model assumes ideal adsorption behavior, in which the adsorption sites are energetically equivalent and no lateral interactions occur between adsorbed molecules, whether the

Table 7 Summary of some previous studies on Ce/CeO_2 and BTA systems as corrosion inhibitors for steel in NaCl solutions

Inhibitor system	Metal/substrate	Medium	Protection efficiency (%)	Main mechanism	Ref.
BTA	20SiMn steel	3.5%.wt NaCl	60%	The chemisorption of BTA through N–Fe bond on the surface	70
CeO_2 NPs	Mild steel	0.1 M NaCl	—	Formation of a passive/conversion layer on the steel surface, leading to a blocking-electrode behavior and delayed corrosion	35
BTA + Na_2HPO_4	Carbon steel	NaCl solutions	94%	Deposited film composed of Fe–BTA complexes and iron phosphates	71
BTA + Co	Mild steel	3.5%.wt NaCl	91%	The formation and precipitation of a BTA–Co chelate layer on the steel surface, acting as a protective barrier	72
CeO_2/PPY/BTA	Epoxy coating/Mild steel	3.5 wt% NaCl	89%	Excellent self-healing	73
BTA-CeO_2 NPs	A1008 carbon steel	3.5%.wt NaCl	93.4%	Deposited BTA film on steel surface, while CeO_2 NPs enhance surface coverage, provide additional adsorption sites, and improve film compactness and stability	This work

process is physical or chemical in nature. The Langmuir isotherm is expressed by eqn (10). Where C_{inh} denotes the inhibitor concentration, θ the surface coverage, and K_{ads} the equilibrium constant of the adsorption–desorption process. Using the surface coverage values (θ) derived from electrochemical measurements (Tafel polarization), the plots of $\frac{C_{inh}}{\theta}$ *versus* C_{inh} are presented in Fig. 13.

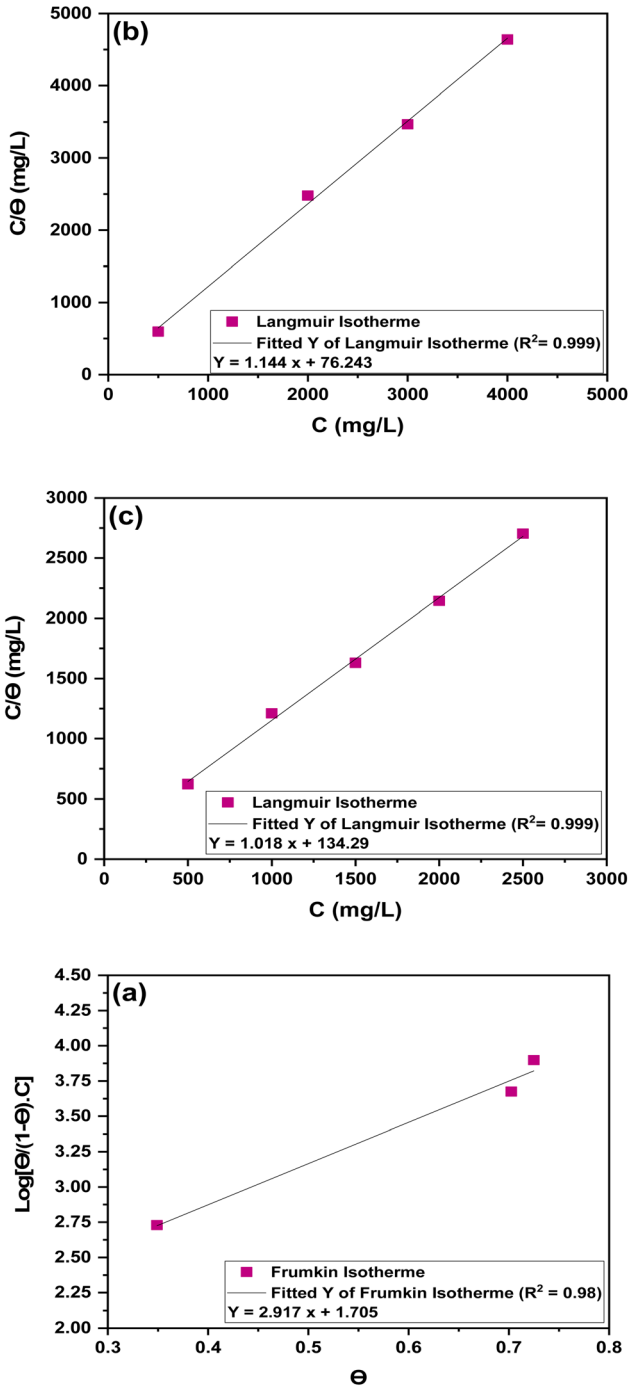

Fig. 13 Adsorption isotherms of (a) CeO_2 NPs, (b) 1*H*-BTA, and (c) 1*H*-BTA–CeO_2 NPs inhibitors on carbon steel, modeled using the Frumkin isotherm for CeO_2 NPs and the Langmuir isotherm for 1*H*-BTA and 1*H*-BTA–CeO_2 NPs inhibitors.

$$\frac{C_{inh}}{\theta} = \frac{1}{K_{ads}} + C_{inh} \quad (10)$$

In parallel, the Frumkin adsorption isotherm describes the equilibrium between inhibitor molecules adsorbed on the metal surface and those remaining in the solution phase. Unlike the Langmuir isotherm, the Frumkin model takes into account lateral interactions among the adsorbed species.[74] The applicability of the Frumkin isotherm is confirmed when a linear relationship is obtained by plotting $\log\left(\frac{\theta}{1-\theta}\right)[C_{inh}]$ as a function of θ, with a slope equal to $\frac{2a}{2.303}$. The corresponding mathematical expression is given by eqn (11):

$$\log\left(\frac{\theta}{1-\theta}\right)[C_{inh}] = \frac{2a}{2.303} + \log K_{ads} \quad (11)$$

where a is the lateral interaction parameter describing the molecular interactions within the adsorbed layer, K_{ads} is the adsorption–desorption equilibrium constant, and C_{inh} is the inhibitor concentration. The adsorption isotherm modeling results indicate that the interaction of the CeO_2 NPs inhibitor with the carbon steel surface follows the Frumkin isotherm, with a correlation coefficient of $R^2 = 0.98$. In contrast, the adsorption of 1*H*-BTA and the 1*H*-BTA–CeO_2 NPs inhibitors on the carbon steel surface conforms to the Langmuir isotherm, with correlation coefficients of $R^2 = 0.99$ and $R^2 = 0.99$, respectively. From both plots of the Frumkin and Langmuir adsorption isotherms, the adsorption equilibrium constant K_{ads} for each studied inhibitor (CeO_2 NPs, 1*H*-BTA and the 1*H*-BTA–CeO_2 NPs) can be determined. This constant reflects the affinity of the inhibitor for the steel surface and can subsequently be used to calculate the standard free energy of adsorption (ΔG^0_{ads}), which provides insight into the strength and nature of the interaction between the inhibitor molecules and the metal surface. The value of (ΔG^0_{ads}) is calculated using the following equations (eqn (12) and (13)):[75,76]

$$K_{ads} = \frac{1}{55.5}\exp\left(\frac{-\Delta G^0_{ads}}{RT}\right) \quad (12)$$

$$\Delta G^0_{ads} = -RT\ln(55.5K_{ads}) \quad (13)$$

In general, values of ΔG^0_{ads} around -20 kJ mol^{-1} or less negative are indicative of physical adsorption (physisorption), which results from electrostatic interactions. In contrast, chemisorption is associated with ΔG^0_{ads} values of -40 kJ mol^{-1} or more negative, reflecting charge sharing or transfer between the inhibitor molecules and the metal surface.[77]

Table 8 shows that the standard free energy of adsorption (ΔG^0_{ads}) is -29.51 kJ mol^{-1} for the CeO_2 NPs inhibitor, -27.70 kJ mol^{-1} for 1*H*-BTA, and -27.22 kJ mol^{-1} for the 1*H*-BTA–CeO_2 NPs hybrid system. These results indicate that CeO_2 NPs, 1*H*-BTA and the 1*H*-BTA–CeO_2 inhibitors are adsorbed onto the carbon steel surface *via* a mixed physico-chemical mechanism, involving both physical and chemical interactions with the metal surface.

Table 8 Thermodynamic adsorption parameters of CeO_2 NPs, 1*H*-BTA, and 1*H*-BTA–CeO_2 NPs inhibitors on carbon steel in 3.5 wt% NaCl solution

	K_{ads} (L. mol^{-1})	ΔG^0_{ads} (kJ. mol^{-1})
CeO_2 NPs	3.27 10^3	−29.51
1*H*-BTA	1.56 10^3	−27.70
1*H*-BTA–CeO_2 NPs	1.28 10^3	−27.22

4. Conclusion

This study establishes the strong corrosion inhibition effect of a hybrid system comprising 1*H*-BTA and CeO_2 NPs on A1008 low carbon steel in a 3.5% NaCl solution. While both inhibitors demonstrated notable individual performance; achieving efficiencies of 74.13% (1*H*-BTA at 2.5 mmol L^{-1}) and 73.35% (CeO_2 NPs at 0.3%); their combination at optimal concentrations (2.5 mmol L^{-1} 1*H*-BTA and 0.2% CeO_2 NPs) delivered a remarkable inhibition efficiency of 93.46% in short term tests, confirming a pronounced hybrid system interaction.

Electrochemical analyses (potentiodynamic polarization and electrochemical impedance spectroscopy) revealed that the hybrid system functions as a mixed-type inhibitor with predominantly anodic control. The hybrid system significantly shifted corrosion potential, suppressed corrosion current density, and enhanced both polarization and charge-transfer resistances. Complementary SEM/EDS characterization confirmed the formation of a uniform, crack-free protective layer enriched with cerium (Ce) and nitrogen (N), indicative of strong adsorption and barrier effects.

Extended immersion tests further validated the durability of this system, maintaining 92.90% inhibition efficiency after 14 days and consistently outperforming either inhibitor used alone. Collectively, these findings highlight the promise of the 1*H*-BTA–CeO_2 NPs system as a sustainable, highly efficient corrosion mitigation strategy for carbon steel in chloride solution, offering both immediate protection and long term stability. The XRD analysis corroborates these findings by confirming the formation and persistence of a protective surface layer.

The thermodynamic values of ΔG^0_{ads} indicate that the adsorption of CeO_2 NPs, 1*H*-BTA and the 1*H*-BTA–CeO_2 NPs system on the carbon steel surface occurs through a mixed physico-chemical mechanism, involving both physical and chemical interactions, highlighting their stronger and more effective surface binding.

Conflicts of interest

There are no conflicts to declare.

Data availability

The data that support the findings of this study are available from the corresponding author upon reasonable request.

References

1 O. Girciene L G, A. Selskis, L. Gudaviciute, A. Selskis, V. Jasulaitiene, S. Sakirzanovas and R. Ramanauskas, The self-healing ability of cerium oxide films on carbon steel, *Chemija*, 2015, **26**, 175e183, DOI: 10.6001/chemija.2015.26.3.6.

2 P. D. Desai, C. B. Pawar, M. S. Avhad and A. P. More, Corrosion inhibitors for carbon steel: A review, *Vietnam J. Chem.*, 2023, **61**, 15–42, DOI: 10.1002/vjch.202200111.

3 A. De Mendonça Santos, T. F. De Almeida, F. Cotting, I. V. Aoki, H. G. De Melo and V. R. Capelossi, Evaluation of castor bark powder as a corrosion inhibitor for carbon steel in acidic media, *Mater. Res.*, 2017, **20**, 492–505, DOI: 10.1590/1980-5373-MR-2016-0963.

4 J. Dávila, K. Paucar, A. Vergara, I. V. Aoki, K. Cancino and J. M. Falcón, Bidens pilosa extract as a corrosion inhibitor on 1008 carbon steel in neutral medium, *J. Electrochem. Sci. Eng.*, 2024, **14**, 321–338, DOI: 10.5599/jese.2331.

5 M. B. Valcarce, C. López and M. Vázquez, The Role of Chloride, Nitrite and Carbonate Ions on Carbon Steel Passivity Studied in Simulating Concrete Pore Solutions, *J. Electrochem. Soc.*, 2012, **95**, C200, DOI: 10.1149/2.006206jes.

6 C. D. Gu, W. Yan, J. L. Zhang and J. P. Tu, Corrosion resistance of AZ31B magnesium alloy with a conversion coating produced from a choline chloride–urea based deep eutectic solvent, *Corros. Sci.*, 2016, **106**, 108–116, DOI: 10.1016/j.corsci.2016.01.030.

7 M. Ezazi, B. Shrestha, N. Klein, D. H. Lee, S. Seo and G. Kwon, Self-healable superomniphobic surfaces for corrosion protection, *ACS Appl. Mater. Interfaces*, 2019, **11**, 30240–30246, DOI: 10.1021/acsami.9b08855.

8 J. Ding, H. Zhao, M. Zhou, P. Liu and H. Yu, Super-anticorrosive inverse nacre-like graphene-epoxy composite coating, *Carbon*, 2021, **81**, 204–211, DOI: 10.1016/j.carbon.2021.05.017.

9 M. Cui, B. Wang and Z. Wang, Nature-inspired strategy for anticorrosion, *Adv. Eng. Mater.*, 2019, **21**, 1801379, DOI: 10.1002/adem.201801379.

10 A. Messabhia, H. Boudellioua, Y. Hamlaoui and F. Pedraza, Electrochemical deposition of graphene-doped polyaniline films for enhanced zinc corrosion resistance, *Appl. Surf. Sci.*, 2025, **701**, 163311, DOI: 10.1016/j.apsusc.2025.163311.

11 H. Boudellioua, Y. Hamlaoui, L. Tifouti and F. Pedraza, Effects of polyethylene glycol (PEG) on the corrosion inhibition of mild steel by cerium nitrate in chloride solution, *Appl. Surf. Sci.*, 2019, **473**, 449–460, DOI: 10.1016/j.apsusc.2018.12.164.

12 A. C. Bastos, M. G. Ferreira and A. M. Simoes, Corrosion inhibition by chromate and phosphate extracts for iron substrates studied by EIS and SVET, *Corros. Sci.*, 2006, **48**, 1500–1512, DOI: 10.1016/j.corsci.2005.05.021.

13 M. Costa and C. B. Klein, Toxicity and carcinogenicity of chromium compounds in humans, *Crit. Rev. Toxicol.*, 2006, **36**, 155–163, DOI: 10.1080/10408440500534032.

14 H. Boudellioua, Y. Hamlaoui, L. Tifouti and F. Pedraza, Corrosion protection mechanism of Ce^{3+}/polyethylene

glycol systems inhibitors for mild steel in sulfate solution, *Mater. Corros.*, 2023, **74**, 1086–1100, DOI: 10.1002/maco.202313727.

15 A. Gharbi, M. Dridi, C. Rémazeilles, Y. Hamlaoui and F. Pedraza, Eco-friendly corrosion inhibition and antioxidant potential of Ficus elastica leaf extract for C1020 carbon steel in acidic medium, *Mater. Today Commun.*, 2025, **47**, 113157, DOI: 10.1016/j.mtcomm.2025.113157.

16 J. A. Mendez, Y. M. Vong and J. Bueno, Cerium and Other Rare Earth Salts as Corrosion Inhibitors—A Review, *Prot. Met. Phys. Chem. Surf.*, 2022, **58**, 801–810, DOI: 10.1134/S2070205122040141.

17 M. M. Mennucci, E. P. Banczek, P. R. P. Rodrigues and I. Costa, Evaluation of benzotriazole as corrosion inhibitor for carbon steel in simulated pore solution, *Cem. Concr. Compos.*, 2009, **31**, 418–424, DOI: 10.1016/j.cemconcomp.2009.04.005.

18 O. A. Goncharova, A. Y. Luchkin, Yu. I. Kuznetsov, N. N. Andreev, N. P. Andreeva and S. S. Vesely, Octadecylamine, 1,2,3-benzotriazole and a mixture thereof as chamber inhibitors of steel corrosion, *Int. J. Corros. Scale Inhib.*, 2018, **7**, 203–212, DOI: 10.17675/2305-6894-2018-7-2-7.

19 Y. I. Kuznetsov, Triazoles as a class of multifunctional corrosion inhibitors. A review. Part I. 1,2,3-Benzotriazole and its derivatives. Copper, zinc and their alloys, *Int. J. Corros. Scale Inhib.*, 2018, **7**, 271–307, DOI: 10.17675/2305-6894-2018-7-3-1.

20 N. P. Andreeva, L. P. Kazanskii, I. A. Selyaninov, Y. I. Kuznetsov and V. A. Ostrovskii, Adsorption of 5-Phenyltetrazole on iron and its inhibition of the dissolution of low-carbon steel in a neutral solution, *Prot. Met. Phys. Chem. Surf.*, 2009, **45**, 806–811, DOI: 10.1134/S2070205109070107.

21 Yu. I. Kuznetsov and L. P. Kazansky, Physicochemical aspects of metal protection by azoles as corrosion inhibitors, *Russ. Chem. Rev.*, 2008, **77**, 219–232, DOI: 10.1070/RC2008v077n03ABEH003753.

22 Y. I. Kuznetsov, A. D. Mercer and J. G. N. Thomas, *Organic Inhibitors of Corrosion of Metals*, Springer, New York, 1996, p. 284, DOI: 10.1007/978-1-4899-1956-4.

23 V. S. Sastri, *Green Corrosion Inhibitors: Theory and Practice*. John Wiley & Sons, Inc, Hoboken, New Jersey, 2011, p. 169, DOI: 10.1002/9781118015438.

24 K. Babić-Samardžija and N. Hackerman, Triazole, benzotriazole and substituted benzotriazoles as corrosion inhibitors of iron in aerated acidic media, *J. Solid State Electrochem.*, 2005, **9**, 483–497, DOI: 10.1007/s10008-004-0584-z.

25 U. Rammelt, S. Koehler and G. Reinhard, Synergistic effect of benzoate and benzotriazole on passivation of mild steel, *Corros. Sci.*, 2008, **50**, 1659–1663, DOI: 10.1016/j.corsci.2008.02.016.

26 J. Saranya, M. Sowmiya, P. Sounthari, K. Parameswari, S. Chitra and K. Senthilkumar, N-heterocycles as corrosion inhibitors for mild steel in acid medium, *J. Mol. Liq.*, 2016, **217**, 335–342, DOI: 10.1016/j.molliq.2015.12.096.

27 N.-B. Huang and C.-H. Liang, Corrosion Behavior of Carbon Steel in Lithium Bromide Solution, *J. Chin. Chem. Soc.*, 2003, **50**, 979–984, DOI: 10.1002/jccs.200300138.

28 S. Liu, N. Xu, J. Duan, Z. Zeng, Z. Feng and R. Xiao, Corrosion inhibition of carbon steel in tetra-n-butylammonium bromide aqueous solution by benzotriazole and Na_3PO_4, *Corros. Sci.*, 2009, **51**, 1356–1363, DOI: 10.1016/j.corsci.2009.03.021.

29 T. Kosec, D. K. Merl and I. Milošev, Impedance and XPS study of benzotriazole films formed on copper, copper–zinc alloys and zinc in chloride solution, *Corros. Sci.*, 2008, **50**, 1987–1997, DOI: 10.1016/j.corsci.2008.04.016.

30 S. M. A. El Haleem, S. A. El Wanees and A. Bahgat, Environmental factors affecting the corrosion behaviour of reinforcing steel. VI. Benzotriazole and its derivatives as corrosion inhibitors of steel, *Corros. Sci.*, 2014, **87**, 321–333, DOI: 10.1016/j.corsci.2014.06.043.

31 K. Sabet Bokati and C. Dehghanian, Adsorption Behavior of 1H-benzotriazole Corrosion Inhibitor on Aluminum alloy 1050, Mild steel and Copper in Artificial Seawater, *J. Environ. Chem. Eng.*, 2018, **6**, 1613–1624, DOI: 10.1016/j.jece.2018.02.015.

32 K. Sabet Bokati, C. Dehghanian and S. Yari, Corrosion inhibition of copper, mild steel and galvanically coupled copper-mild steel in artificial sea water in presence of 1H-benzotriazole, sodium molybdate and sodium phosphate, *Corros. Sci.*, 2017, **126**, 272–285, DOI: 10.1016/j.corsci.2017.07.009.

33 M. Petrunin, L. Maksaeva, N. Gladkikh, Y. Makarychev, M. Maleeva, T. Yurasova and A. Nazarov, Thin Benzotriazole Films for Inhibition of Carbon Steel Corrosion in Neutral Electrolytes, *Coatings*, 2020, **10**, 362, DOI: 10.3390/coatings10040362.

34 R. Sharmila, N. Selvakumar and K. Jeyasubramanian, Evaluation of corrosion inhibition in mild steel using cerium oxide nanoparticles, *Mater. Lett.*, 2013, **91**, 78–80, DOI: 10.1016/j.matlet.2012.09.051.

35 M. Fedel, A. Ahniyaz, L. G. Ecco and F. Deflorian, Electrochemical investigation of the inhibition effect of CeO_2 nanoparticles on the corrosion of mild steel, *Electrochim. Acta*, 2014, **131**, 71–78, DOI: 10.1016/j.electacta.2013.11.164.

36 N. Bourenane, Y. Hamlaoui and F. Pedraza, Electrochemical investigation of ceria nanoparticles as a corrosion inhibitor for steel in alkaline medium, *Mater. Corros.*, 2023, **74**, 1356–1370, DOI: 10.1002/maco.202313821.

37 H. H. Zhang, X. Zhang, H. Bian, L. Zhang, Y. Chen, Y. Yang and Z. Zhang, Benzotriazole loaded CeO_2 nano-containers towards superior anti-corrosive silane coating for protection of copper, *Colloids Surf. A Physicochem. Eng. Aspects.*, 2024, **682**, 132844, DOI: 10.1016/j.colsurfa.2023.132844.

38 X. Han, R. Guo, B. Niu and H. Yan, Enhanced corrosion resistance of epoxy resin coating via addition of CeO_2 and

benzotriazole, *Chin. J. Chem. Eng.*, 2024, **67**, 89–96, DOI: 10.1016/j.cjche.2023.11.021.

39 J. Yang, B. Zou, Q. Fang, J. Wang and L. Wang, BTA loaded in various CeO_2 nanocontainers in epoxy coating for long-term anticorrosion of low carbon steel, *Prog. Org. Coat.*, 2022, **172**, 107156, DOI: 10.1016/j.porgcoat.2022.107156.

40 *ASTM G44-21. Standard Practice for Exposure of Metals and Alloys by Alternate Immersion in Neutral 3.5% Sodium Chloride Solution*. ASTM International, West Conshohocken, PA, USA, 2021, DOI: 10.1520/G0044-21.

41 S. Salmi, H. Boudellioua, Y. Hamlaoui and M. Fedel, Evaluating the Corrosion Inhibition Performance of Cerium Oxide/Cerium Nitrate Inhibitors on Carbon Steel in Chloride Solutions, *Mater. Corros.*, 2025, **76**, 1780–1800, DOI: 10.1002/maco.70020.

42 R. Tantra, S. Jing, S. K. Pichaimuthu, *et al*, Dispersion stability of nanoparticles in ecotoxicological investigations: the need for adequate measurement tools, *J. Nanopart. Res.*, 2011, **13**, 3765–3780, DOI: 10.1007/s11051-011-0298-y.

43 H. Y. Chang and H. I. Chen, Morphological Evolution for CeO_2 Nanoparticles Synthesized by Precipitation Technique, *J. Cryst. Growth*, 2005, **283**, 457–468, DOI: 10.1016/j.jcrysgro.2005.06.002.

44 M. Stern and A. L. Geary, Electrochemical polarization: I. A theoretical analysis of the shape of polarization curves, *J. Electrochem. Soc.*, 1957, **104**, 56–63, DOI: 10.1149/1.2428496.

45 K. Zhang, B. Xu, W. Yang, X. Yin, Y. Liu and Y. Chen, Halogen-substituted imidazolinederivatives as corrosion inhibitors for mild steel in hydrochloric acid solution, *Corros. Sci.*, 2015, **90**, 284–295, DOI: 10.1016/j.corsci.2014.10.032.

46 I. B. Onyeachu and M. M. Solomon, Benzotriazole derivative as an effective corrosion inhibitor for low carbon steel in 1 M HCl and 1 M HCl + 3.5 wt% NaCl solution, *J. Mol. Liq.*, 2020, **313**, 113536, DOI: 10.1016/j.molliq.2020.113536.

47 D. Wanga, C. Pan, Z. Liu, K. Chen, N. Chen and S. Liu, Synergetic effect of two inhibitors for enhanced corrosion protection on the reinforcing steel in the chloride-contaminated carbonated solutions, *Constr. Build. Mater.*, 2021, **286**, 122916, DOI: 10.1016/j.conbuildmat.2021.122916.

48 T. Kosec, I. Milosev and B. Pihlar, Benzotriazole as an inhibitor of brass corrosion in chloride solution, *Appl. Surf. Sci.*, 2007, **253**, 8863–8873, DOI: 10.1016/j.apsusc.2007.04.083.

49 R. Li, S. Yabe, M. Yamashita, S. Momose, S. Yoshida, S. Yin and T. Sato, Synthesis and UV-Shielding Properties of ZnO- and CaO-doped CeO_2 via Soft Solution Chemical Process, *Solid State Ionics*, 2002, **151**, 235–241, DOI: 10.1016/S0167-2738(02)00715-4.

50 L. G. Ecco, S. Rossi, F. Deflorian and M. Fedel, Electrochemical Behavior of AA5005 Aluminum Alloy in Acidic Chloride-Based Medium Containing CeO_2 Nanoparticle, *J. Electrochem. Soc.*, 2018, **165**, C86, DOI: 10.1149/2.0371814jes.

51 S. R. Kunst, H. R. P. Cardoso, L. V. R. Beltrami, *et al*, New Sol-Gel Formulations to Increase the Barrier Effect of a Protective Coating Against the Corrosion and Wear of Galvanized Steel, *Mater. Res.*, 2015, **18**, 138–150, DOI: 10.1590/1516-1439.288914.

52 C. Li, Z. Peng and J. Huang, Impedance Response of Electrochemical Interfaces: Part IVLow-Frequency Inductive Loop for a Single-Electron Reaction, *J. Phys. Chem. C*, 2023, **127**, 16367–16373, DOI: 10.1021/acs.jpcc.3c02830.

53 A. P. Hanza, R. Naderi, E. Kowsari and M. Sayebani, Corrosion behavior of mild steel in H_2SO_4 solution with 1,4-di [1′-methylene-3′-methyl imidazolium bromide]-benzene as an ionic liquid, *Corros. Sci.*, 2016, **107**, 96–106, DOI: 10.1016/j.corsci.2016.02.023.

54 D. Song, J. Wang, H. Guan, S. Zhang, Z. Zhou and S. Zhang, Enhanced Corrosion Resistance of Carbon Steel Rebar in Chloride-Containing Water Solutions: The Role of Lotus Extract in Corrosion Inhibition, *Metals*, 2025, **15**, 510, DOI: 10.3390/met15050510.

55 H. Boudellioua, Y. Hamlaoui, L. Tifouti and F. Pedraza, Comparison Between the Inhibition Efficiencies of Two Modification Processes With PEG–Ceria Based Layers Against Corrosion of Mild Steel in Chloride and Sulfate Media, *J. Mater. Eng. Perform.*, 2017, **26**, 4402–4414, DOI: 10.1007/s11665-017-2867-4.

56 U. Donatus, J. V. de Sousa Araujo, C. de Souza Carvalho Machado, N. V. Vardhan Mogili, R. A. Antunes and I. Costa, The Effect of Manufacturing Process Induced Near-Surface Deformed Layer on the Corrosion Behaviour of AA2198-T851 Al–Cu–Li Alloy, *Corros. Eng., Sci. Technol.*, 2019, **54**, 205–215, DOI: 10.1080/1478422X.2018.1558932.

57 M. Gobara, A. Baraka, R. Akid and M. Zorainy, Corrosion Protection Mechanism of Ce^{4+}/Organic Inhibitor for AA2024 in 3.5% NaCl, *RSC Adv.*, 2020, **10**, 2227–2240, DOI: 10.1039/C9RA09552G.

58 K. Aramaki and N. Hackerman, Inhibition Mechanism of Medium-Sized Polymethyleneimine, *J. Electrochem. Soc.*, 1969, **116**, 568–574, DOI: 10.1149/1.2411965.

59 L. B. Coelho, D. Cossement and M. G. Olivier, Benzotriazole and cerium chloride as corrosion inhibitors for AA2024-T3: An EIS investigation supported by SVET and ToF-SIMS analysis, *Corros. Sci.*, 2018, **130**, 177–189, DOI: 10.1016/j.corsci.2017.11.004.

60 A. M. Abdel-karim, R. A. Azzam, O. El-Said Shehata, A. Mohamed, O. A. A. El-Shamy and G. A. El mahdy, Electrochemical performance of a novel 1-(benzo[d]thiazol-2-yl)-3-methylguanidine as effective corrosion inhibitor for carbon steel in 1 M hydrochloric acid, *Sci. Rep.*, 2025, **15**, 28196, DOI: 10.1038/s41598-025-12838-2.

61 Y. I. Kuznetsov, Physicochemical aspects of metal corrosion inhibition in aqueous solutions, *Russ. Chem. Rev.*, 2004, **73**, 75–87, DOI: 10.1070/RC2004v073n01ABEH000864.

62 C. Verma, R. Kumar, S. Singh, P. Sharma, A. Gupta and M. Yadav, Corrosion inhibition of mild steel in 1 M HCl by D-glucose derivatives of dihydropyrido [2,3-d:6,5-d′] dipyrimidine-2,4,6,8(1H,3H,5H,7H)-tetraone, *Sci. Rep.*, 2017, **7**, 44432, DOI: 10.1038/srep44432.

63 U. Trdan, A. Logar, D. Klobčar, I. Milošev, B. Kapun and P. Rodič, Corrosion mitigation of AA6082, Copper-ETP, and

their galvanic couple using $Ce(OAc)_3$, Na_2SO_4, and 1H-BTA in chloride solution, *J. Mater. Res. Technol.*, 2026, **40**, 2422–2436, DOI: 10.1016/j.jmrt.2025.12.290.

64 F. F. Eliyan, E. S. Mahdi and A. Alfantazi, Electrochemical Evaluation of the Corrosion Behaviour of API-X100 Pipeline Steel in Aerated Bicarbonate Solutions, *Corros. Sci.*, 2012, **58**, 181–191, DOI: 10.1016/j.corsci.2012.01.015.

65 C. N. Cao and J. Q. Zhang, *An Introduction to Electrochemical Impedance*, Science Press. Beijing, 2002, China 1-17.

66 L. Huang, Q. Luo and Y. He, Assessment of Corrosion Protection Performance of $FeOOH/Fe_3O_4/C$ Composite Coatings Formed In Situ on the Surface of Fe Metal in Air-Saturated 3.5 wt.% NaCl Solution, *Materials*, 2023, **16**, 224–235, DOI: 10.3390/ma16010224.

67 F. Cao, J. Li, M. Liu, J. Lv, X. Dong, W. Wang, T. Wang, Q. Fan and Y. Liu, Outstanding synergistic inhibition effect of $Ca_3(PO_4)_2$ and BTA on Q235 steel in NaCl solution, *Corros. Eng., Sci. Technol.*, 2025, DOI: 10.1177/1478422X251360180.

68 X. Liu, C. Gu, Z. Wen and B. Hou, Improvement of active corrosion protection of carbon steel by water-based epoxy coating with smart CeO_2 nanocontainers, *Prog. Org. Coat.*, 2018, **115**, 195–204, DOI: 10.1016/j.porgcoat.2017.10.015.

69 F. Cao, G. Gao, J. Li, T. Li, Z. He, T. Wang, Y. Liu, Q. Fan, H. Ma and X. Chen, First-principles and experimental study on the inhibition efficiency of BTA for 20SiMn steel in chloride-containing solutions, *Mater. Lett.*, 2023, **352**, 135164, DOI: 10.1016/j.matlet.2023.135164.

70 D. Wang, C. Pan, Z. Liu, K. Chen, N. Chen and S. Liu, Synergetic effect of two inhibitors for enhanced corrosion protection on the reinforcing steel in the chloride-contaminated carbonated solutions, *Constr. Build. Mater.*, 2021, **301**, 122916, DOI: 10.1016/j.conbuildmat.2021.122916.

71 H. Akhavan, M. Izadi, I. Mohammadi, T. Shahrabi and B. Ramezanzadeh, The synergistic effect of BTA–Co system on the corrosion inhibition of mild steel in 3.5 wt% NaCl solution, *J. Electrochem. Soc.*, 2018, **165**, C670–C679, DOI: 10.1149/2.1111810jes.

72 S. Khokher and S. Lata, Benzotriazole loaded polypyrrole/cerium oxide synthesized composite blend within epoxy resin designed as superior coatings against mild steel oxidative corrosion in sodium chloride medium, *J. Mol. Struct.*, 2024, **1312**, 138525, DOI: 10.1016/j.molstruc.2024.138525.

73 A. H. Alamri and I. B. Obot, Highly efficient corrosion inhibitor for C1020 carbon steel during acid cleaning in multistage flash (MSF) desalination plant, *Desalination*, 2019, **470**, 114100, DOI: 10.1016/j.desal.2019.114100.

74 P. C. Okafor and Y. Zheng, Synergistic inhibition behaviour of methylbenzyl quaternary imidazoline derivative and iodide ions on mild steel in H_2SO_4 solutions, *Corros. Sci.*, 2009, **51**, 850–859, DOI: 10.1016/j.corsci.2009.01.027.

75 M. E. Belghiti, S. Bouazama, S. Echihi, A. Mahsoune and A. Elmelouky, Understanding the adsorption of newly benzylidene–aniline derivatives as a corrosion inhibitor for carbon steel in hydrochloric acid solution: Experimental, DFT and molecular dynamic simulation studies, *Arab. J. Chem.*, 2020, **13**, 1499–1519, DOI: 10.1016/j.arabjc.2017.12.003.

76 A. Zarrouk, B. Hammouti, H. Zarrok, S. S. Al-Deyab and M. Messali, Temperature effect, activation energies and thermodynamic adsorption studies of L-cysteine methyl ester hydrochloride as copper corrosion inhibitor in Nitric Acid 2M, *Int. J. Electrochem. Sci.*, 2011, **6**, 6261–6274, DOI: 10.1016/S1452-3981(23)19679-9.

77 X. Zheng, S. Zhang, W. Li, M. Gong and L. Yin, Experimental and theoretical studies of two imidazolium-based ionic liquids as inhibitors for mild steel in sulfuric acid solution, *Corros. Sci.*, 2015, **95**, 168–179, DOI: 10.1016/j.corsci.2015.03.012.